JOURNAL OF GEOPHYSICAL RESEARCH, VOL. 113, C07029, doi:10.1029/2007JC004562, 2008

Infragravity waves in the deep ocean: Generation, propagation, and seismic hum excitation

Yusuke Uchiyama[1] and James C. McWilliams[1]

Received 19 September 2007; revised 7 February 2008; accepted 26 March 2008; published 22 July 2008.

[1] Oceanic infragravity waves are investigated as a possible source of seismic free oscillations, often referred to as the "hum" of the Earth, using a numerical model of depth-independent, nondispersive, long-wave dynamics with a forcing from nonlinear interactions among the primary wind waves (including swell). Because of near-resonant amplification, the structure of the primary-wave forcing field in shallow water, and an edge-trapping mechanism, infragravity waves are excited very effectively near the coasts. Deep-water infragravity waves are significantly influenced both by offshore leakage and propagation of the coastally generated free waves and by deep-water primary-wave forcing. With the inclusion of "mesoscale" variability on top of the more slowly varying primary waves generated in synoptic storms, the deep-water infragravity waves are found to have an amplitude on the order of a millimeter in height, which is consistent with field observations and considered to be sufficient to account for local hum excitation in the middle of the basin.

Citation: Uchiyama, Y., and J. C. McWilliams (2008), Infragravity waves in the deep ocean: Generation, propagation, and seismic hum excitation, *J. Geophys. Res.*, *113*, C07029, doi:10.1029/2007JC004562.

1. Introduction

[2] Seismologists have detected Earth's hum, *i.e.*, low-frequency seismic free oscillations in discrete frequencies between 2 and 7 mHz that occur even on seismically quiet days [*Nawa et al.*, 1998; *Suda et al.*, 1998]. The frequencies of the free oscillation coincide with spheroidal fundamental modes of Earth, distinct from the microseismic noise at frequencies peaked near 0.2 Hz. The amplitude of hum is typically equivalent to about a magnitude 6.0 earthquake every day [*Tanimoto and Um*, 1999; *Ekström*, 2001]. The source of the hum must be near Earth's surface because the fundamental modes are all Rayleigh waves. Since the hum occurs continuously, it cannot be explained by intermittent large earthquakes nor by summing the contributions of small earthquakes [*Tanimoto et al.*, 1998]. The likely cause is pressure fluctuations in the air or water at their bottom solid surface. Microseisms are known to be caused by oceanic surface wind waves (*i.e.*, "primary" waves, inclusive of remotely generated swell) that generate pressure fluctuations that do not wane with depth [*Longuet-Higgins*, 1950]. The same mechanism is not applicable to the generation of the much lower frequency hum. Some researchers have speculated that atmospheric disturbances distributed uniformly over both land and sea surface are a possible source of hum [*Kobayashi and Nishida*, 1998; *Tanimoto and Um*, 1999; *Nishida et al.*, 2000; *Ekström*, 2001]. Recently, *Rhie and Romanowicz* [2004] used two arrays of broadband seismometers in California and Japan to detect the propagation of Rayleigh waves during 2000. The strongest incident Rayleigh waves originate in the Northern Pacific during the boreal winter and in the southern ocean in the austral winter. These are sites of especially strong storms and associated wind waves. This implicates the mechanism of nonlinear interaction among wind waves to generate long, low-frequency, oceanic infragravity waves, rather than atmospheric pressure fluctuations [*e.g.*, *Webb et al.*, 1991; *Webb*, 1998; *Tanimoto*, 2005; *Webb*, 2007]. Estimating the size of seafloor pressure from existing measurements, *Tanimoto* [2005] found sufficient energy in the infragravity fluctuations to excite the observed seismic signals. *Rhie and Romanowicz* [2006] extended their earlier analysis to compare the data from the seismic arrays with a global wave analysis and showed that one source of hum was located along the U.S. West Coast during the winter of 2000. They proposed that some coastal infragravity waves locally generate bottom pressure fluctuations, while others propagate long distances and generate fluctuations throughout the basin. The resulting low-frequency seismic waves propagate over the globe and constitute the hum.

[3] The theory of infragravity waves shows they are generated by nonlinear interactions among the primary waves, have depth-independent horizontal-velocity and pressure profiles, and propagate as nondispersive shallow-water waves [*e.g.*, *Hasselmann*, 1962; *Longuet-Higgins and Stewart*, 1962; *McWilliams et al.*, 2004]. As part of the same interactions, modulations of primary wave height also induce a bound or quasi-static depression of the sea level (*i.e.*, wave set-up). Observed alongshore wave number spectra [*Munk et al.*, 1964; *Huntley et al.*, 1981; *Oltman-*

[1]Institute of Geophysics and Planetary Physics, University of California, Los Angeles, California, USA.

0148-0227/08/2007JC004562$09.00

Shay and Guza, 1987], weak energy levels in the deep ocean [*Webb et al.*, 1991], and cross-shore amplitude variations [*Okihiro et al.*, 1992] all suggest that infragravity waves are refractively trapped on the shelf as edge modes with only weak radiation to the deep ocean. Various models suggest that free waves are generated close to shore [*e.g.*, *Longuet-Higgins and Stewart*, 1962; *Gallagher*, 1971; *Bowen and Guza*, 1978; *Foda and Mei*, 1981; *Symonds et al.*, 1982], but the processes controlling the spatial and temporal variability of infragravity waves are still poorly understood. Because of their greater amplitude and instrumental accessibility, observations of infragravity waves have been made mostly on continental shelves [*e.g.*, *Munk*, 1949; *Tucker*, 1950; *Guza and Thornton*, 1982; *Okihiro et al.*, 1992; *Herbers et al.*, 1994, 1995a, 1995b; *Sheremet et al.*, 2002]. In this nearshore context infragravity waves are involved in surf beats, edge waves, foreshore beach erosion during storms, formation of cuspate topography, harbor oscillations, *etc*. Fewer measurements have been made for infragravity waves in the deep ocean. The main reason is that the amplitude of deep-water infragravity wave is extremely small and thus hard to measure accurately. For instance, *Webb et al.* [1991] reported maximum amplitudes of deep-water infragravity waves inferred from bottom pressure sensors ranging from $O(10^{-4})$ m in the Atlantic to $O(10^{-3})$ m in the Pacific, although the sampling was quite sparse. They also found that deep-water infragravity wave energy is correlated not with the local wind-wave energy but with swell energy averaged over all coastlines from which free infragravity waves could originate. Furthermore, *Rhie and Romanowicz* [2006] suggest the hum is generated in deep water partly by freely propagating infragravity waves generated near the shoreline.

[4] *Webb* [2007] proposed a weakly nonlinear spectral theory on coupling between ocean waves and seismic modes by extending the microseismic excitation theory by *Longuet-Higgins* [1950] and *Hasselmann* [1963], relying on weak wave triads for energizing very low-frequency difference waves on the continental shelves. He approximately reproduces the seismic spectrum observed, and confirmed that ocean waves, rather than atmospheric turbulence, are driving the seismic modes of Earth. However, this mechanism is somewhat doubtful for producing very low frequency long waves from interacting primary waves with nearly equal frequencies, since that requires phase coherence of the primary waves over the longer time and distance of the product long wave (*n.b.*, this objection is not as cogent for shorter infragravity waves like surf beats). Instead, we make use of the more robust multiscale theory [*McWilliams et al.*, 2004] where the long-wave response is forced by the spectrum-integrated primary-wave properties.

[5] This paper is aimed at clarifying the dynamics of infragravity waves in the deep ocean that are due to local and remote excitation by primary gravity waves whose wave-averaged properties vary with ''synoptic''-scale storms and with finer, ''mesoscale'' fluctuations. The latter forcing comprises empirically demonstrated modulations of the primary-wave-averaged forcing on an intermediate mesoscale, longer than the primary waves but shorter than the meteorological synoptic scale. Particular issues are distinguishing the responses either bound to the forcing field or freely propagating, assessing the degree of wave confinement by topography near the coastline, and examining the relative efficiencies of coastal and abyssal infragravity wave generation. By the generation mechanism we study, the frequencies of interest are defined by those of the hum itself. Therefore we have not pursued surf beats, shear waves, nearshore infragravity waves, ~100 s wave-envelope modulations relevant to surf-zone infragravity waves, nor any of the other motions with frequencies only moderately lower than those of wind waves and swells (typically higher than 40 mHz) observed in surf zones. Nevertheless, since the infragravity waves have their maximum amplitudes at the shoreline, we incorporate subgrid-scale forcing modulations due to refraction and breaking in shallow water based on a simplified WKB model with an empirical breaking parameterization. This approach enables us to investigate deep-ocean infragravity long-waves with a relatively large grid spacing, $\sim O(10^3)$ m. This focus on lower-frequencies and longer-scales phenomena allows us to accurately rely on the nondispersive shallow-water approximation. We can further reply on a linear wave-response dynamics where each spectrum component of the primary wavefield modulation at any scales independently forces its own response because of the observed (and simulated) small long-wave amplitude of $\sim O(10^{-3})$ m. Therefore we investigate this problem with a newly developed numerical model based on a barotropic version of ROMS [Regional Oceanic Modeling System; *Shchepetkin and McWilliams*, 2005]. A linearized long-wave equation with general topography and shoreline shape and with primary-wave-averaged forcing derived in a multiscale, asymptotic wave-current interaction theory by *McWilliams et al.* [2004] is used to represent infragravity waves on regional and basin scales.

2. Infragravity-Wave Dynamics

[6] Long (infragravity) waves are driven by nonlinear interaction among primary waves, whose sea level amplitude η_p varies on a fast wave-scale $(\mathbf{x}, t)$. η_p is written in a Fourier integral representation as

$$\eta_p(\mathbf{x},t) = \int_{-\infty}^{\infty} \hat{\eta}_p(\mathbf{k};\mathbf{X},\tau)\exp[i\{\mathbf{k}\cdot\mathbf{x}-\omega t\}]d\mathbf{k}, \qquad (1)$$

along with the linear dispersion relation,

$$\omega^2(\mathbf{k}) = gk\tanh[kh]. \qquad (2)$$

ω is a radian frequency; $k = |\mathbf{k}| = 2\pi/L$ is the magnitude of the horizontal wave number vector $\mathbf{k}$; and $h(\mathbf{X})$ is the resting water depth. The caret, $\hat{\cdot}$, denotes the complex amplitude of each Fourier component. As in the asymptotic analysis of *McWilliams et al.* [2004] (MRL04), we assume the waves have a slowly varying envelope dynamics in the horizontal and time coordinates $(\mathbf{X}, \tau)$, where $\mathbf{X} = \beta\mathbf{x}$, $\tau = \beta t$, and $\beta \ll 1$, including a long-wave component that does not oscillate on the scale of the primary wave coordinates $(\mathbf{x}, t)$. The forced, dissipative long-wave equations adapted from MRL04 are

$$\frac{\partial \mathbf{q}}{\partial \tau} + g\nabla\tilde{\zeta} = \mathcal{D}, \quad \frac{\partial \tilde{\zeta}}{\partial \tau} + \nabla\cdot(h\mathbf{q}) = \mathcal{F}. \qquad (3)$$

$\mathcal{D} = -C_d\,\mathbf{q}/h$ is the bottom drag force with a linear friction coefficient C_d, and $\mathcal{F}$ is the nonlinear infragravity-wave forcing averaged over the primary waves:

$$\mathcal{F} = -\left[\nabla\cdot\left(\frac{A^2\omega\mathbf{k}}{2k\,\tanh\,kh}\right)^{\dagger} - \frac{\partial}{\partial\tau}\left(\frac{A^2k}{2\,\sinh\,2kh}\right)^{\dagger}\right] \tag{4}$$

$$= -\left[\nabla\cdot\left(\frac{E}{\rho c}\frac{\mathbf{k}}{k}\right)^{\dagger} - \frac{\partial}{\partial\tau}\left(\frac{E}{\rho g h}\left\{\frac{c_g}{c_p} - \frac{1}{2}\right\}\right)^{\dagger}\right] \tag{5}$$

$$= -\left[\nabla\cdot\mathbf{T}^{St} + \frac{\partial\zeta^s}{\partial\tau}\right]. \tag{6}$$

$\tilde{\zeta}$ is the long-wave, free-surface elevation, and $\mathbf{q}$ is the associated, depth-independent horizontal velocity. $(\cdot)^{\dagger}$ denotes a band-pass filtering operator, averaging over the primary waves and excluding slower variations on the scale of oceanic currents (not modeled in this paper). A is wave amplitude; $c_g = \partial\omega/\partial k$ is group velocity; and $c_p = \omega/k$ is phase speed. Both c_g and c_p are associated with propagation in the direction of $\mathbf{k}$. The quantities $\mathbf{T}^{St}$ and ζ^s in $\mathcal{F}$ are the vertically integrated Stokes drift (*i.e.*, Stokes transport) and the quasi-static sea level response, often called the set-up. The wave energy per unit area is

$$E = \frac{1}{2}\rho g A^2. \tag{7}$$

[7] The alternative expressions for $\mathcal{F}$ are written for a single Fourier component in η_p, and the contributions can be superimposed for multiple components.

3. Spectral Representation of Wave-Averaged Quantities

[8] The primary wavefield η_p is described by a two-dimensional (2D) wave number spectra $G(\mathbf{k};\,\mathbf{X},\,\tau)$ on the wave-averaged scales. G is nonzero only for $\mathbf{k}$ values within the primary wave range, and the wave properties such as amplitude and spectrum shape change over the slowly varying coordinates $(\mathbf{X},\,\tau)$. In this study we will make use of the global 2D frequency-directional wave spectral reanalysis provided by ECMWF [ERA-40, *cf. Bidlot et al.*, 2002; *Janssen et al.*, 1997], $G(\omega,\,\theta)$, at each point in their analysis (a 1.5° geographical grid), where θ is the wave number vector direction. The ECMWF wave analysis is made four times a day by the WAM cycle-4 global wave model with data assimilation. G is discretized with 25 frequency bins and 12 directional bins.

[9] The local variance of η_p is represented using the spectrum as

$$\overline{\eta_p^2}(\mathbf{X},\tau) = \int_0^{\infty}\int_{-\pi}^{\pi} G(\omega,\theta;\mathbf{X},\tau)\,d\theta\,d\omega, \tag{8}$$

with

$$G(\omega,\theta;\mathbf{X},\tau) = \frac{2\pi k G(\mathbf{k};\mathbf{X},\tau)}{\partial\omega/\partial k} \tag{9}$$

is an alternative representation of $G(\mathbf{k})$ using the dispersion relation [*Komen et al.*, 1994] (Figure 1, left). The mean wave period T_m and mean wave direction θ_m are evaluated with G by

$$T_m(X,\tau) = 2\pi\frac{\displaystyle\int_0^{\infty}\int_{-\pi}^{\pi} G(\omega,\theta;\mathbf{X},\tau)\,d\theta\,d\omega}{\displaystyle\int_0^{\infty}\int_{-\pi}^{\pi}\omega G(\omega,\theta;\mathbf{X},\tau)\,d\theta\,d\omega}, \tag{10}$$

$$\theta_m(\mathbf{X},\tau) = \tan^{-1}\frac{\displaystyle\int_0^{\infty}\int_{-\pi}^{\pi}\sin\theta G(\omega,\theta;\mathbf{X},\tau)\,d\theta\,d\omega}{\displaystyle\int_0^{\infty}\int_{-\pi}^{\pi}\cos\theta G(\omega,\theta;\mathbf{X},\tau)\,d\theta\,d\omega}. \tag{11}$$

[10] The Stokes transport and the wave set-up in (6) can be calculated in spectral form [*Kenyon*, 1969, 1970; *Battjes*, 1972]:

$$\mathbf{T}^{St}(\mathbf{X},\tau) = \int_0^{\infty}\int_{-\pi}^{\pi}\frac{G(\omega,\theta;\mathbf{X},\tau)\omega\mathbf{k}(\omega,\theta)}{2k(\omega)\tanh k(\omega)h(\mathbf{X})}\,d\theta\,d\omega \tag{12}$$

$$\zeta^s(\mathbf{X},\tau) = -\int_0^{\infty}\int_{-\pi}^{\pi}\frac{G(\omega,\theta;\mathbf{X},\tau)k(\omega)}{2\,\sinh\,2k(\omega)h(\mathbf{X})}\,d\theta\,d\omega. \tag{13}$$

4. Mesoscale Forcing Modulation

[11] We can further express the slow-wave number and -frequency dependencies for wave-averaged properties such as E, $\mathbf{T}^{St}$, and ζ^s through a Fourier transform into $(\mathbf{K},\,\Omega)$ space (Figure 1, right). For example,

$$\mathbf{T}^{St}(\mathbf{X},\tau) = \int_{-\infty}^{\infty}\int_{-\infty}^{\infty}\hat{\mathbf{T}}^{St}(\mathbf{K},\Omega)e^{i\{\mathbf{K}\cdot\mathbf{X}-\Omega\tau\}}\,d\mathbf{K}\,d\Omega, \tag{14}$$

and no dispersion relation is implied between Ω and $\mathbf{K}$. Since these are primary-wave-averaged quantities, the spectral variance vanishes in the primary wave frequency band ω_p, but there is variance at lower frequencies associated with storms (Ω_s) and even with climate variability. The spatial and temporal resolution of the ECMWF wave analysis, on what we call the synoptic scale, is rather coarse: $\Delta\tau$ = 6 h and ΔX = 1.5°. However, the primary wave properties vary on even finer scales that we call the mesoscale, with $\Omega_s < \Omega_m < \omega_p$. There is no information about the mesoscale component in the ECMWF analysis. We formally separate these slowly varying components, *e.g.*,

$$\mathbf{T}^{St}(\mathbf{X},\tau) = \mathbf{T}_s^{St}(\mathbf{X},\tau) + \mathbf{T}_m^{St}(\mathbf{X},\tau); \tag{15}$$

the subscripts s and m stand for the synoptic and the mesoscale components.

[12] A crude representation for the slowly varying $(\mathbf{X},\,\tau)$ behaviors is to collapse the full primary-wave spectrum in G into a single primary-wave component (denoted by subscript p) with an equivalent primary wave sea level variance $\overline{A^2}/2$. Practically speaking, the primary wavefield quantities that matter for forcing the long waves (*i.e.*, $\mathbf{T}^{St}$ and ζ^s, both

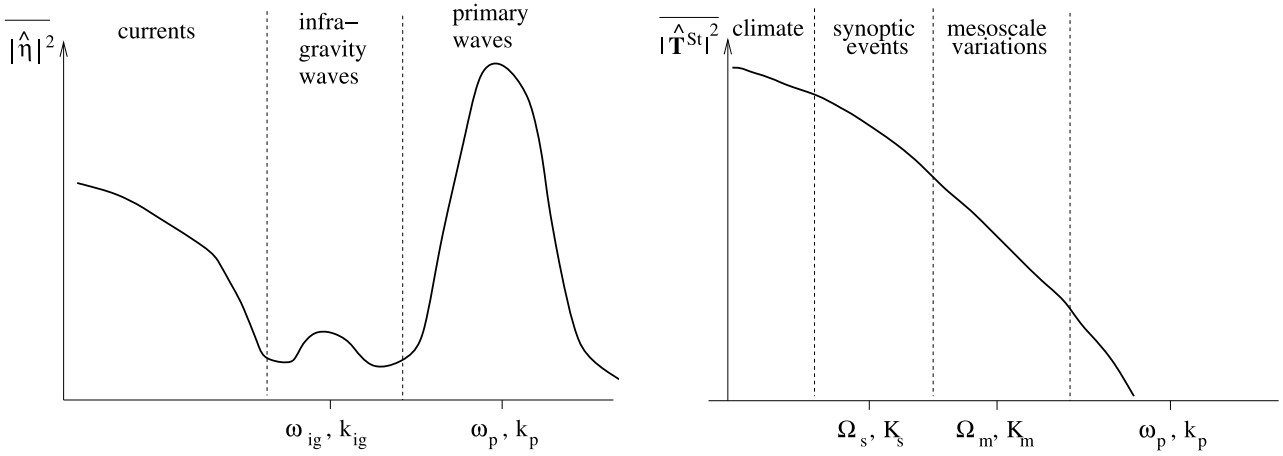

Figure 1. Schematic diagrams of different scale ranges in the frequency ω or horizontal wave number k spectra for sea-surface elevation η (left) or for the wave-averaged Stokes transport $\mathbf{T}^{St}$ (right). The primary-wave frequency spectrum $G(\omega)$ corresponds to the right peak in the left plot, and the slowly varying time and space dependencies in $G(\mathbf{X}, \tau)$ contribute in the right plot to the slowly varying wave number-frequency Ω-K spectrum. Infragravity-wave signals in $\tilde{\zeta}$ and ζ^s appear as the middle peak in the left plot.

of which have very steep spectra at high frequency or wave number for a typical surface elevation spectrum, as evident in their definitions in (5)) have almost all their variance from the primary-wave spectrum peak component, not the shorter, faster components in the primary wave spectrum, so their is nothing important lost by representing the primary wavefield by its peak component. It is reasonable to identify ω_p with $2\pi/T_m$ and θ_p with θ_m from (10) and (11). The slowly varying fields can be expressed with separate synoptic and mesoscale components associated with separate amplitudes, A_s and A_m,

$$\begin{aligned} A(\mathbf{X},\tau) &= A_s(\mathbf{X},\tau) + A_m(\mathbf{X},\tau), \\ &\equiv A_s(\mathbf{X},\tau)\cdot[1+\delta_m(\mathbf{X},\tau)]. \end{aligned} \tag{16}$$

δ_m is defined as the nondimensional fractional amplitude of the mesoscale component. Since we require $A > 0$ and analyze the synoptic wave variability with $A_s > 0$, $|\delta_m| < 1$. A further simplification is to assume that the primary wave properties vary only on the synoptic scale, except for the wave amplitude that varies on both synoptic and mesoscales. With both these simplifications the synoptic and mesoscale contributions to the Stokes transport are expressed as

$$\mathbf{T}_s^{St}(X,\tau) \approx \frac{A_s^2\omega_p}{2\tanh k_p h}\left[\cos\theta_p,\ \sin\theta_p\right], \tag{17}$$

$$\mathbf{T}_m^{St}(\mathbf{X},\tau) \approx \left(2\delta_m + \delta_m^2\right)\mathbf{T}_s^{St}. \tag{18}$$

[13] An analogous expression to (18) can be given for ζ^s, and together these comprise the necessary forcing fields for equation (3). For the basin-scale experiment in the later sections, we estimate $\mathbf{T}^{St}$ and ζ^s using the ECMWF-ERA40 spectral wave data.

[14] Furthermore, a similar collapse of the mesoscale variability spectrum can be made into a single Fourier component, again with an amplitude variance equivalent to the spectrum integral over the mesoscale band. The observed small long-wave amplitude, $\sim O(10^{-3})$ m, allows us to use a linear wave-response dynamics that means that each spectrum component of the primary wave modulation (mesoscale and synoptic) independently forces its own response. Thus the response to a broadband modulation field is merely the linear superposition of the independent component responses, and there is nothing to be gained by constructing a broadband mesoscale forcing that cannot be learned by using representative mesoscale components and demonstrating how the long wave response depends on their amplitude and wave number. There is even the interpretive advantage of isolating representative spectrum components since that allows a clear demonstration of how their properties influence the response (note that influence of "multidirectional" mesoscale variations is briefly examined with a realistic, basin-scale configuration in section 11 and Appendix E).

[15] If the mesoscale component has a spatial wave number $K_m = 2\pi/\lambda_m$, where λ_m is a wavelength of mesoscale fluctuations, then

$$\delta_m(\mathbf{X},\tau) = \delta_0 \sin[\mathbf{K}_m\cdot\mathbf{X} - \Omega_m\tau], \tag{19}$$

$$\delta_m(\mathbf{X},\tau) = K_m c^{gr}, \tag{20}$$

$$\mathbf{K_m}(\mathbf{X},\tau) = \left[K_m\cos\theta_p, K_m\sin\theta_p\right]. \tag{21}$$

$0 < \delta_0 < 1$ is the relative magnitude of the mesoscale amplitude. Ω_m is the mesoscale oscillation frequency determined by the theoretical expectation that mesoscale

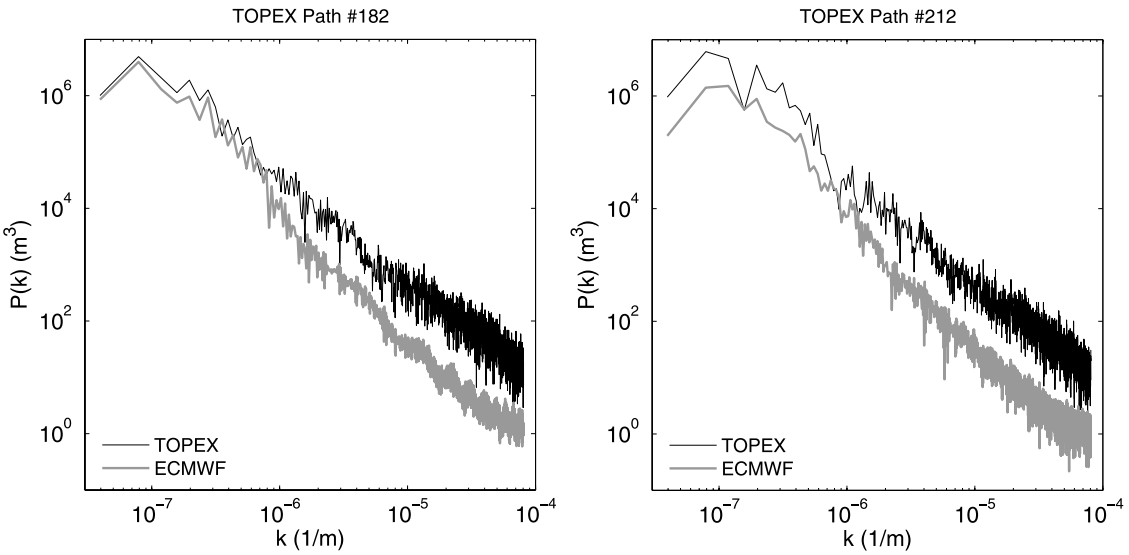

Figure 2. Wave number spectra of significant wave height estimated with the TOPEX altimeter in the Pacific Ocean averaged over cycles 269 through 272 (January–February 2000). (Left) Along Path #182 (eastern Pacific) and (right) Path #212 (western Pacific). Also shown are ECMWF wave analyses linearly interpolated for the same time and place as the TOPEX data.

variations in primary wave energy propagate with the group speed of the dominant primary wave with $k = k_p$,

$$c^{gr}(\mathbf{X},\tau) = \frac{\partial\omega}{\partial k}(k_p) = \frac{\omega_p(k_p)}{2k_p}\left(1 + \frac{2k_p h}{\sinh 2k_p h}\right). \qquad (22)$$

The mesoscale forcing propagation direction coincides with the primary phase propagation direction θ_p. Note that reflection of the meso- and synoptic-scale disturbances from the shoreline is not considered in the present forcing formalism.

[16] In calculating the infragravity-wave response to the mesoscale forcing, we will choose K_m^{-1} somewhat arbitrarily as shorter than the scales resolved in the ECMWF analysis but larger than the grid scale of our model, viewing it as a control parameter. On the other hand, an estimate for the fractional amplitude δ_0 is evaluated using a combination of TOPEX/Poseidon satellite radar altimetry (http://topex-www.jpl.nasa.gov), the National Data Buoy Center (NDBC) pitch-roll buoy data (http://www.ndbc.noaa.gov), and the ECMWF global wave reanalysis (http://www.ecmwf.int/research/era). Band-integrated synoptic and mesoscale sea level variances are calculated from these sources and

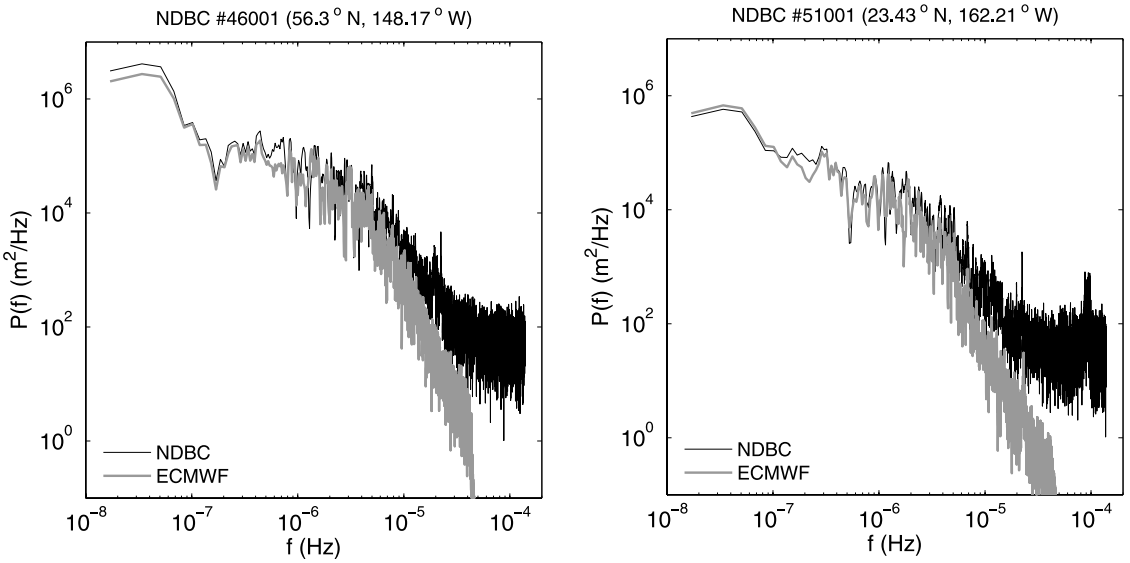

Figure 3. Frequency spectra of significant wave height, H_s, measured by NDBC wave buoys and the corresponding ECMWF reanalysis at two locations in Pacific Ocean for the year 2000: (left) #46001 near Alaska and (right) #51001 near Hawaii.

Table 1. Primary-Wave Amplitude Variances, $\overline{A^2}$, and Mean Amplitude, $\bar{A}$, From the TOPEX and ECMWF Wave Data[a]

	Cycle	269	270	271	272
$\overline{A^2}$ (m^2)	ECMWF	0.3945	0.3064	0.3355	0.3754
	TOPEX	0.6001	0.4933	0.5166	0.6132
	mesoscale	0.0088	0.0079	0.0075	0.0085
$\bar{A}$ (m)	ECMWF	0.8120	0.7409	0.7458	0.7958
	TOPEX	1.0073	0.9383	0.9291	1.0126
	mesoscale	0.1260	0.1216	0.1192	0.1250
δ_0		0.1552	0.1641	0.1599	0.1571

[a] $\overline{A^2}$ and $\bar{A}$ are estimated by taking averages of wave number spectra along all the satellite paths that span the Pacific Ocean integrated over each TOPEX cycles, #269–#272.

averaged over the available samples, yielding $\overline{A_2^2}$ and $\overline{A_m^2}$ (see also Appendix A). This leads to the estimator,

$$\delta_0 = \left(\frac{\overline{A_m^2}}{\overline{A_s^2}}\right)^{1/2}. \tag{23}$$

[17] TOPEX/Poseidon data provides the significant wave height of the ocean surface directly underneath the satellite with an accuracy of about ±0.1–0.2 m [*Callahan et al.*, 1994]. The altimeter wave height has a finer spatial spatial resolution about 6 km along the satellite paths than that of the ECMWF's reanalysis (*i.e.*, 1.5°) while temporal resolution is coarse since the repeat period of the satellite orbit is about 10 d. On the contrary, NDBC provides significant wave height once every hour with an accuracy of ±0.2 m, although the buoys are sparsely distributed in space.

[18] Figure 2 compares wave number spectra of spatial distributions of significant wave height measured by the TOPEX radar altimetry along the paths 182 and 212 (both in Pacific Ocean), averaged over Cycles 269 to 272 in January and February 2000, and their counterparts estimated with the ECMWF reanalysis. By applying the cut-off wave number using the ECMWF grid spacing in the spectral domain to extract the synoptic and mesoscale fluctuations, we obtain reference values for δ_0 from (23) as summarized in Table 1. Similarly, Figure 3 shows frequency spectra of significant wave height measured by the two wave buoys deployed in the Pacific Ocean and from the ECMWF's reanalysis. Table 2 is their summary. The comparison between the measurements and reanalysis gives us δ_0 ranging from 0.076 to 0.263, suggesting that δ_0 can be a function of time and space. By averaging these estimates, δ_0 may be reduced to a single mean value, $\delta_0 \approx 0.16$ that we will use in the present study because observations of mesoscale wave variability, in particular wave groups in the deep ocean, are rare [*n.b.*, synthetic aperture radars have recently begun to be utilized for detecting variability of wave groups; *Nieto Borge et al.*, 2004].

5. Nearshore Forcing

[19] The primary waves vary significantly in shallow water near the shoreline because of refraction, shoaling, and breaking. This is relevant to the wave-averaged forcing $\mathcal{F}$ in (6). However, the width of this nearshore zone is often small compared to the regional and basin scales that are our focus, so special care must be taken with the representation of its effects in a more coarsely resolved model. In addition, nearshore infragravity waves are most energetic at the shoreline and are important for exciting the hum on continental shelves, as documented empirically by *Rhie and Romanowicz* [2006], and rationalized theoretically by *Webb* [2007]. Instead of ignoring the surf zone effects totally as *Webb* [2007] did, we have incorporated the minimum effects of wave breaking and associated modification of the nearshore forcing into our model as described below.

[20] We take the view that the offshore wavefield is specified as described in sections 3–4, and $\mathbf{k}_p$ and $\overline{\eta_p^2}$ are modified near the coast using ray theory, an empirical breaking parameterization, and grid-scale averaging. In combination with the dispersion relation (2), ray theory [*e.g.*, *Lighthill*, 1978; *Mei*, 1989] implies

$$\frac{\partial \mathbf{k}}{\partial \tau} + \nabla\omega = 0, \quad \nabla \times \mathbf{k} = 0, \quad \frac{\partial \mathcal{A}}{\partial \tau} + \nabla\left(c_g \mathcal{A}\right) = -\frac{\epsilon_b}{\omega}. \tag{24}$$

$\mathcal{A} = E/\omega$ is the wave action, and ϵ_b is dissipation rate of wave energy E due to breaking. In applying these equations near the coast, we assume that the primary wavefield is locally steady and represented by its equivalent monochromatic wave; alongshore derivatives of the local topography and wave number vector are negligible compared to cross-shore derivatives; and shoreline reflection is unimportant. Then the ray equations reduce to

$$\nabla\omega = \frac{d\omega}{dx_\perp} = 0, \quad \frac{dk_\parallel}{dx_\perp} = 0, \quad \frac{d}{dx_\perp}\left(c_g^{(x_\perp)} E\right) = -\epsilon_b, \tag{25}$$

Table 2. Primary-Wave Amplitude Variances, $\overline{A^2}$, and Mean Amplitude, $\bar{A}$, Evaluated by Integrating Frequency Spectra of the NDBC and ECMWF Wave Height Variations for the Eight Locations in Pacific Ocean Measured for a Year in 2000

buoy #		46001	46002	46006	46035	46059	46066	51001	51028
Longitude, °W		104.17	86.36	93.48	133.58	86.00	110.98	118.21	109.87
Latitude, °N		56.30	42.58	40.80	57.05	37.98	52.70	23.43	0.02
$\overline{A^2}$ (m^2)	ECMWF	0.6967	0.5727	0.7019	0.7516	0.4081	1.0620	0.1952	0.0418
	NDBC	1.1155	0.8237	0.9110	1.0831	0.7543	1.1612	0.2756	0.0529
	mesoscale	0.0124	0.0064	0.0066	0.0579	0.0115	0.0062	0.0127	0.0029
$\bar{A}$ (m)	ECMWF	1.1804	1.0703	1.1848	1.2260	0.9035	1.4574	0.6248	0.2890
	NDBC	1.4937	1.2835	1.3498	1.4718	1.2282	1.5240	0.7425	0.3253
	mesoscale	0.1573	0.1129	0.1150	0.3402	0.1518	0.1114	0.1594	0.0761
δ_0		0.1332	0.1055	0.0971	0.2775	0.1680	0.0764	0.2551	0.2634

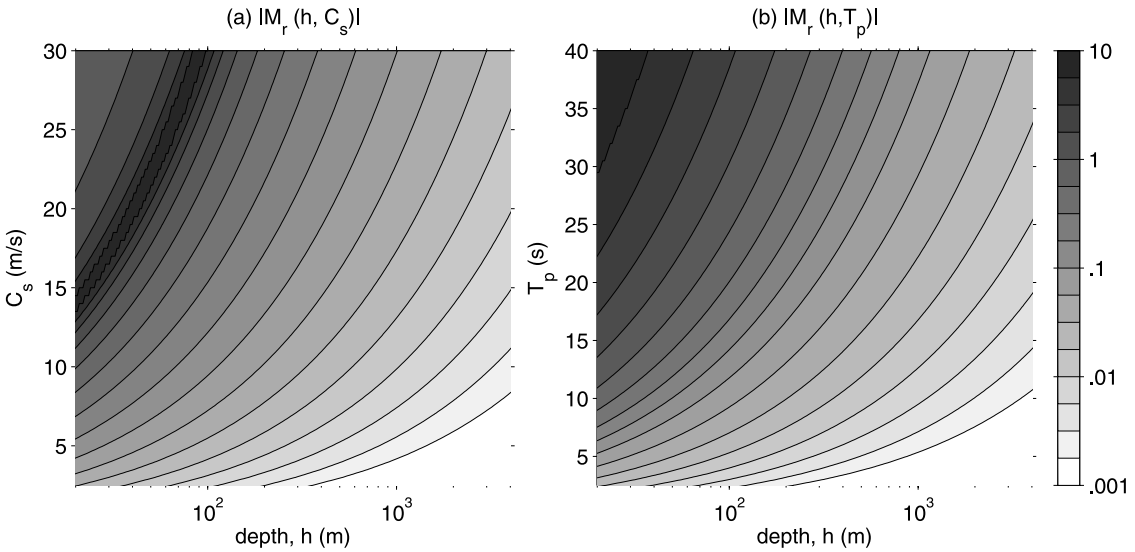

Figure 4. Analytical amplification factor $|\mathcal{M}_r|$ from (29) as a function of depth h and forcing phase speed U_f. (Left) phase speed of the synoptic storm, C_s, and (right) group speed of primary wave (*i.e.*, phase speed of the mesoscale forcing) c^{gr} computed from the primary wave period T_p. Both synoptic and mesoscale forcings are capable of inducing resonant amplification in shallow water ($h < O(10^2)$ m), but the deep-water response is always off-resonant.

where $x_\perp$ denotes the cross-shore spatial coordinate and $k_\parallel$ is the alongshore wave number component. Equation (25) implies that ω and $k_\parallel$ are constant approaching the shoreline. We can use the dispersion relation and the known topographic shoaling profile $h(x_\perp)$ to determine the horizontal wave number magnitude $k(x_\perp)$, hence the perpendicular wave number component $k_\perp(x_\perp)$ and the wave number angle relative to the shoreline. Shoaling $h(x_\perp)$ generally implies increasing $k(x_\perp)$ and turning of the ray toward the shoreline. When $\epsilon_b = 0$ (*i.e.*, outside the surf zone), (7) and (25) imply that

$$\frac{A^2\sqrt{k_\parallel^2 + k_\perp^2}}{c_g k_\perp} \equiv \mathcal{P}_\infty \tag{26}$$

is constant along a ray and independent of $x_\perp$ approaching the shoreline, and with (22) this yields a formula for $A(x_\perp)$. As h decreases, A generally increases since c_g decreases. Within the surf zone where wave breaking occurs and $\epsilon_b \neq 0$, we assume that the wave amplitude is limited to be a fraction of the local depth,

$$A(x_\perp) = \frac{1}{2}\gamma h(x_\perp). \tag{27}$$

This simple parameterization is generally supported according to laboratory experiments [*cf. Battjes*, 1972] with $\gamma = 0.73$ [*Battjes and Stive*, 1985]. By this rule, as $h(x_\perp)$ decreases, $A(x_\perp)$ must also decrease, which is the opposite of the shoaling effect in (26). So our shallow-water prescription for $A(x_\perp)$ is to take the minimum value between the two expressions (26) and (27).

[21] In discretization of the forcing term (6), we have found it necessary to apply a local averaging and smoothing operator in evaluating $\mathcal{F}$ (Appendix B). This is both because the composite rule for $A(x_\perp)$ has a discontinuous cross-shore derivative where its two expressions match and because $\mathcal{F}$ has a singular amplitude as $h \to 0$. The net result is reasonably satisfactory in limiting the sensitivity to the grid size and the shallowest depth near the shoreline $h_{\min}$.

6. Resonant Amplification

[22] In this section we evaluate an analytical solution to the forced long-wave equation (3) in a simplified setup, *viz.*, one-dimensional (1D) problems with flat bottom topography and no bottom friction. The governing equations reduce to

$$\tilde{\zeta}_{\tau\tau} - c^2\tilde{\zeta}_{XX} = -Z_{\tau\tau}, \qquad Z_{\tau\tau} = -\int^\tau \mathcal{F} d\tau. \tag{28}$$

$c = \sqrt{gh}$ is the phase speed of long waves, and X denotes the spatial coordinate. We consider a moving disturbance $Z = Z(X, \tau)$ in the primary wavefield with a specified propagation speed U_f. The particular solution to (28) is designated by $\tilde{\zeta} = \mathcal{M}_r Z$, where $\mathcal{M}_r$ is an amplification factor in the response; hence,

$$\mathcal{M}_r = \left(1 - U_f^2/c^2\right)^{-1}. \tag{29}$$

Thus the resonance condition to (29) is $c = \pm U_f$, consistent with that by *Longuet-Higgins and Stewart* [1962] based on the radiation stress formalism for long waves generation. In deep water a characteristic depth is about 4000 m so that $c \approx 200$ m/s, whereas a typical U_f due to synoptic storm is about 10 m/s. The group speed of a deep-water primary-waves (*i.e.*, the phase speed of mesoscale forcing), c^{gr}, is also approximately 10 m/s. Either case gives rise to $U_f \ll c$, so the long-wave response $\tilde{\zeta}$ is always off-resonant and quasi-static in deep water.

[23] Equation (28) also provides a free-wave solution if appropriate boundary conditions are given [*e.g.*, *Proudman*,

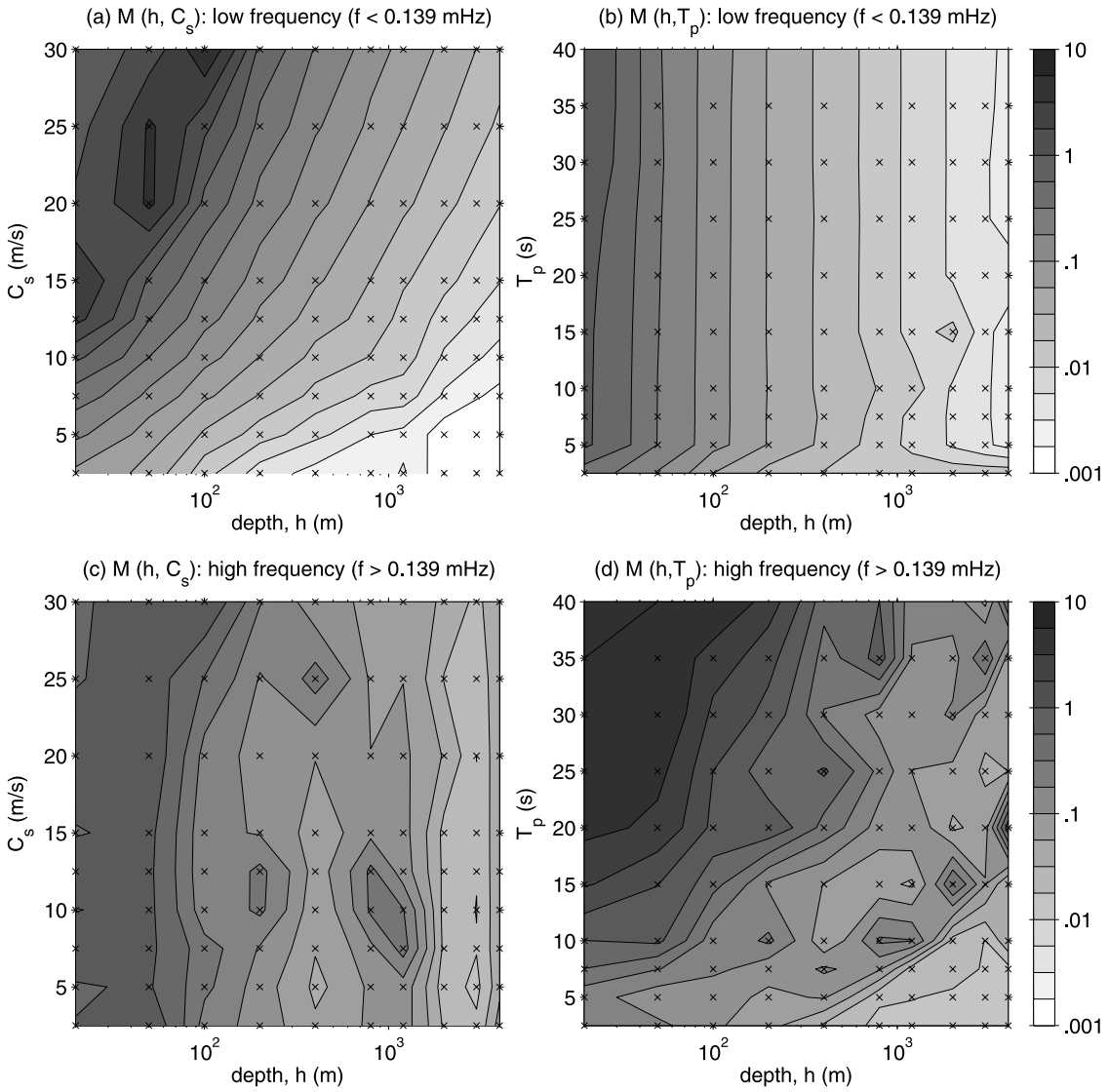

Figure 5. Amplification factor $\mathcal{M}$ in the same format as Figure 4 for (a–b) low-frequency band ($f < 0.139$ mHz) and (c–d) high-frequency band ($f \geq 0.139$ mHz) evaluated from (32) with 1D solutions with a flat bottom. The cross marks denote discrete forcing conditions for the calculations. Overall the pattern of $\mathcal{M}$ resembles $|\mathcal{M}_r|$ in Figure 4.

1953]. Suppose that there is a shoreline at $X = 0$ such that barotropic velocity is $q(0, \tau) = 0$, and Z moves toward the shoreline. Then we obtain the general solution of (28) as a sum of the particular solution (above) and a general solution of the homogeneous form of (28):

$$\tilde{\zeta} = \mathcal{M}_r \left[Z(\tau - X/U_f) - \frac{U_f}{c} Z(\tau - X/c) \right]. \qquad (30)$$

[24] This equation illustrates that in shallow water, where the response to the traveling disturbance Z comes close to resonant condition, there are two types of response: 1) bound (slaved) waves that travel with the forcing field and 2) free waves that propagate at a phase speed of $c = \sqrt{gh}$. Figure 4 shows $|\mathcal{M}_r|$ as a function of depth h, a phase speed of synoptic storm C_s, and a primary wave period T_p, which is relevant to the phase speed of mesoscale forcing, c^{gr}. Hence the forcing phase speed U_f in (29) is given by C_s or $c^{gr}(h, T_p)$. Long waves are excited intensively in shallow water either by synoptic storms or mesoscale forcing, if $h < O(10^2)$ m.

[25] Next, a series of one-dimensional (1D), nondissipative, forced long-wave experiments with a flat bottom is conducted to reproduce resonant response to given synthetic forcing fields. The forcing imposed here is a combination of a synoptic-scale storm traveling at a phase speed of C_s and mesoscale forcing amplitude modulation as described in section 4 with $\lambda_m = 20$ km and $\delta_0 = 0.16$. A total of 10 depths ranging from 20 to 4000 m are chosen to represent the flat topography to cover from shallow to deep water conditions. The length of the domain is 256 km with a grid spacing of 1 km. The initial condition is a resting state. A periodic condition is applied to $\tilde{\zeta}$ and $\mathbf{q}$ at the two open

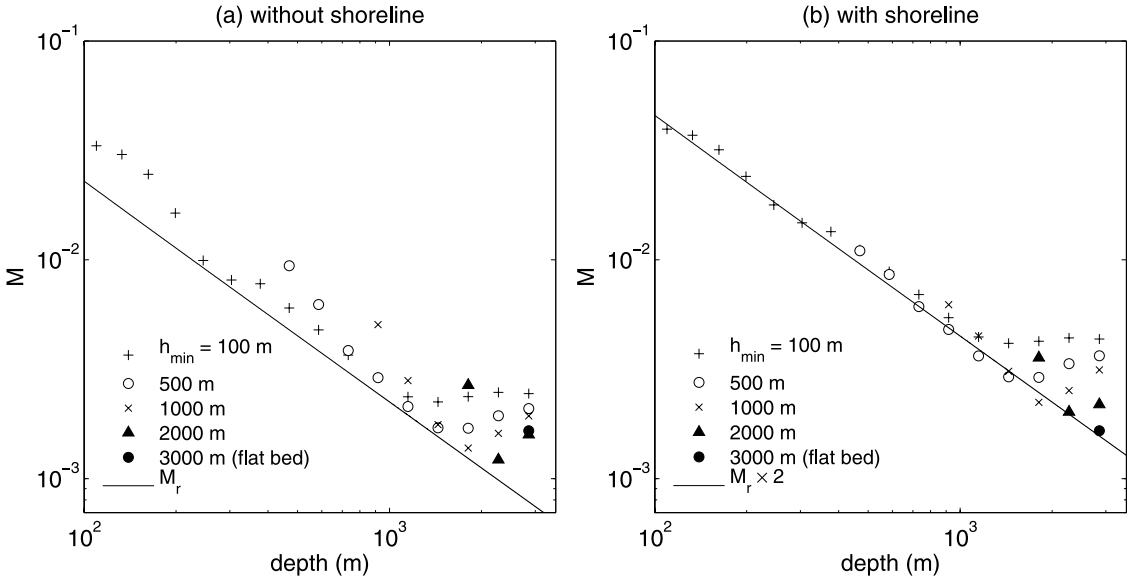

Figure 6. Amplification factor $\mathcal{M}$ for the high-frequency band ($f > 0.1$ mHz) calculated from (32) with the 2D, nonbreaking cases for constant-slope cross-shore topographies: (a) without and (b) with a shoreline by applying a Flather-type radiation condition and a flux-blocking condition on the shallowest side of the domain. The bottom slopes change with the minimum depth of the domain $h_{\min}$ while the offshore maximum depth is fixed at $h_{\max} = 3000$ m. The resonant parameter $|\mathcal{M}_r|$ with $T_p = 6$ s (*i.e.*, $c^{gr} \approx 5$ m/s in deep water) is indicated by the solid curves to demonstrate that $|\mathcal{M}_r|$ is close to $\mathcal{M}$. Including the shoreline increases the response by a factor of 2 due to shoreline reflections.

boundaries. The primary wave amplitude A_s resulting from a synoptic storm traveling in the X direction is defined as

$$A_s(X,\tau) = A_0 + A_f \cos(K_s X - \Omega_s \tau), \tag{31}$$

where A_0 and A_f are the mean and fluctuating amplitudes (= 3.25 and 1.75 m, respectively). The storm wavelength is $\lambda_s = 2\pi/K_s = 256$ km, and $C_s = \Omega_s/K_s$ is its phase speed equivalent to the group speed of the primary waves as represented by (22) with a primary wave period, T_p, and the linear dispersion relation (2). We conduct 1D simulations with ten T_p ranging from 2.5 to 40 s with a constant C_s (= 10 m/s), and ten C_s values ranging from 1 to 30 m/s with a constant T_p (= 10 s) for each of the ten flat topographies; hence a total of 200 configurations are examined.

[26] An amplification factor $\mathcal{M}$ is calculated from the numerical solutions to compare with the theoretical estimate $\mathcal{M}_r$:

$$\mathcal{M} = \frac{\langle \tilde{\zeta}_{R.M.S.} \rangle}{\left\langle \int^{\tau} \mathcal{F} d\tau|_{R.M.S.} \right\rangle}. \tag{32}$$

$\tilde{\zeta}_{R.M.S.}$ and $\int^{\tau} \mathcal{F}\, d\tau|_{R.M.S.}$ are standard deviations of the response $\tilde{\zeta}$ and time-integrated forcing $\int^{\tau} \mathcal{F} d\tau$ computed at each grid point for 14 h after the model reaches steady state (about 12 h after the initiation of the model). $\langle\cdot\rangle$ denotes a spatial-averaging operator.

[27] Figure 5 shows 1D solutions expressed by $\mathcal{M}$. $\mathcal{M}$ for the low-frequency band exposes synoptic-scale responses, and the high-frequency band approximately represents the mesoscale responses. Figure 5a is seemingly similar to Figure 4a, and Figure 5d resembles Figure 4, demonstrating that long-wave responses to the given forcing at an arbitrary depth are well approximated by the simple expression $|\mathcal{M}_r|$ in (29). For example, $\mathcal{M}$ tends to have the maximum not at the shallowest depth but slightly deeper (Figures 4a and 5a), since $|\mathcal{M}_r|$ and $\mathcal{M}$ peak where $\sqrt{gh} = C_s$ (*e.g.*, a peak appears at $h \approx 40$ m if $C_s = 20$ m/s). On the contrary, $\mathcal{M}$ monotonically increases as depth decreases, being the largest at the shallowest part (Figure 5b). The overall pattern of $\mathcal{M}$ in Figure 5b,c is essentially independent of T_p and C_s.

[28] These results clearly indicate that the low-frequency and high-frequency responses are amplified according to C_s and $c^{gr}(h, T_p)$, respectively: the mesoscale fluctuations in the forcing are responsible only for high-frequency mesoscale responses, while synoptic-scale variability in the forcing induces low-frequency responses. The forcing phase speed U_f due to synoptic storms (C_s) and mesoscale fluctuations (c^{gr}) are both important parameters that control resonant amplification of the infragravity waves.

7. Deep-Water Generation

[29] Next we extend the 1D flat-bottom experiments to 2D cases on variable topographies in nonbreaking, deep-water conditions for the primary waves. The 2D topographies employed here are planar beaches with constant slopes in the cross-shore (X) direction but uniform in the alongshore (Y) direction, expressed by the following equation:

$$h(X,Y) = h_{\max} - (h_{\max} - h_{\min})X/X_L, \tag{33}$$

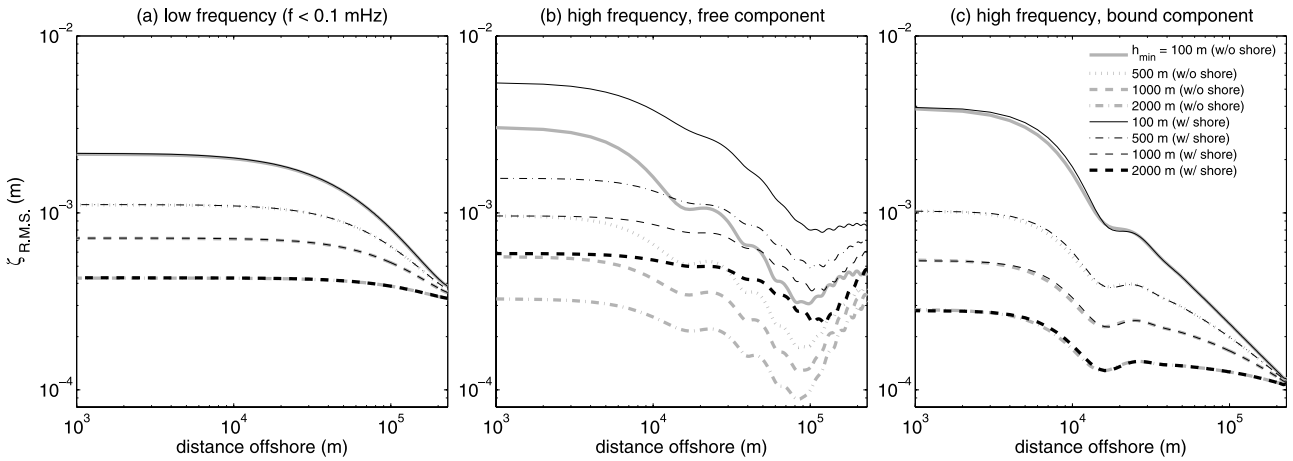

Figure 7. Free-surface response $\tilde{\zeta}_{R.M.S.}$ as a function of offshore distance for the 2D, deep-water experiments with nonbreaking forcing, for various $h_{\min}$ as used in (33). $\tilde{\zeta}_{R.M.S.}$ is decomposed into (a) low-frequency variations ($f < 0.1$ mHz), (b) high-frequency ($f > 0.1$ mHz) infragravity free propagation, and (c) high-frequency bound response. The first four cases in the legend in (c) are without a shoreline, while the others have a shoreline. The shoreline modifies only the infragravity free component.

where $h_{\max} = 3000$ m is the maximum depth at the seaward boundary $X = 0$; $h_{\min}$ is minimum depth at the shoreward boundary $X = X_L$; and X_L is the lateral length of the domain. The domain is set to be 256 × 256 km, discretized with a uniform grid spacing of 1 km. The linear drag coefficient C_d is set to 1.0×10^{-3} m/s. We impose $h_{\min} = 100$, 500, 1000, 2000, and 3000 m (flat bottom). A periodic condition is applied in the alongshore Y direction, while a Flather-type radiation condition is adapted at the seaward boundary, $X = 0$. Two types of the shoreward boundary condition are considered at $X = X_L$: the Flather-type radiation condition so that the domain has no solid boundary, and a flux-blocking condition to make the shoreward boundary be a more complete shoreline. The alongshore periodic forcing is imposed by a traveling synoptic storm at a phase speed, $C_s = \Omega_s/K_s = 10$ m/s, and the wavelength of the traveling storm is $\lambda_s = 2\pi/K_s = 256$ km. A mesoscale amplitude variation is further considered on top of the synoptic-scale forcing, with $\lambda_m = 20$ km and $\delta_0 = 0.16$.

[30] The amplitude of the synoptic storm, A_s, at the offshore-most position is defined as

$$A_s(0, Y, \tau) = A_0 + A_f \cos(K_s Y - \Omega_s \tau). \tag{34}$$

A_0 and A_f are a mean amplitude (= 3.25 m) and a fluctuating amplitude (= 1.75 m). On the contrary, primary wave period and direction are set as constants, *i.e.*, $T_p = 6$ s and $\theta_p = 30°$. Changes in wave number and wave amplitude in the cross-shore direction are computed based on the WKB theory described in Section 5 and Appendix B. The minimum depth $h_{\min} = 100$ m and primary wave period $T_p = 6$ s lead to $kh > 11.17$; hence, all the experiments are in deep-water conditions. None of the cases here involves primary-wave breaking (section 8).

[31] Figure 6 displays the amplification factor, $\mathcal{M}$, defined by (32), for the high-frequency band (*i.e.*, frequency $f > 0.1$ mHz) as a function of depth. The analytically derived resonance parameter, $|\mathcal{M}_r|$, given by (29) with $U_f = c^{gr}(h, T_p)$ is also plotted by the solid curves. $2 \times |\mathcal{M}_r|$ is shown in Figure 6b to approximately account for reflected waves from the shoreline [*Sheremet et al.*, 2002]. Since the primary waves are in deep water ($kh \gg 1$), the R.M.S. forcing is independent of the water depth. $\mathcal{M}$ (thus the response $\tilde{\zeta}$) appears to increase remarkably as depth decreases either with or without the shoreline. The analytically derived $|\mathcal{M}_r|$ is broadly consistent with the $\mathcal{M}$ estimated from the numerical solutions; so the amplification mechanism discussed in section 6 is also relevant to 2D wave excitation on sloping topographies.

[32] We further apply a 2D frequency-alongshore wave number (Ω-K_Y) FFT band-pass filter in order to separate the high-frequency component of the simulated responses into a free propagation and a forced response that are bound to the high-frequency, mesoscale forcing. A combination of the cut-off frequency and wave number is defined by a phase speed of alongshore infragravity waves, $c_Y = \Omega/K_Y = 10.0$ m/s. This filter works well to decompose the high-frequency signals into free propagation and bound response if $h > 10$ m since the phase speed of the free propagation should be $c = \sqrt{gh} > 10$ m/s, although the bound component travels at $c = c_g$, *i.e.*, group speed of the primary wave, which is about 5 m/s for the given primary wave period (*i.e.*, $T_p = 6$ s). A combination of a high-pass frequency filter and 2D Ω-K_Y filter is used to extract the three response components in the 2D regional-scale simulations.

[33] The decomposed response components are plotted against the offshore distance in Figure 7: (1) low-frequency synoptic components, (2) high-frequency free propagation ($f > 0.1$ mHz), and (3) high-frequency bound components. Inclusion of the shore produces evident differences in $\tilde{\zeta}_{R.M.S.}$ for only the high-frequency free component, not the other two components. Although the bound response is equivalent to the free response in shallow water, it decreases sharply as depth increases and the free components make a greater contribution to $\tilde{\zeta}_{R.M.S.}$ in deep water than the bound component. Thus free wave propagation from the shore can

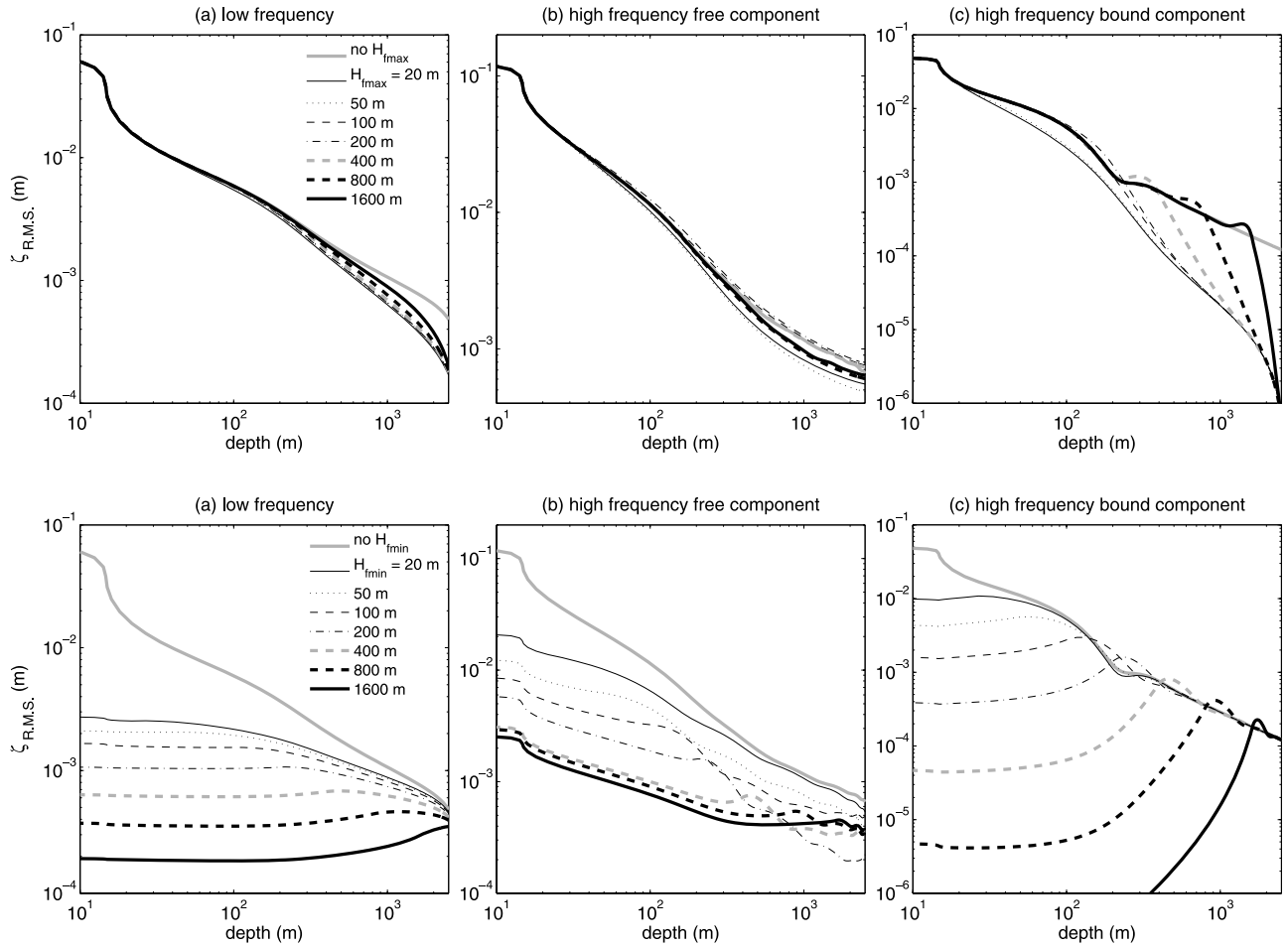

Figure 8. Long-wave response $\tilde{\zeta}_{R.M.S.}$ decomposed for (a) low-frequency band ($f < 0.1$ mHz), (b) high-frequency (infragravity) free-propagation component, and (c) high-frequency bound component for the alongshore-uniform, idealized regional topography with several values for $H_{f\max}$ (upper) and $H_{f\min}$ (lower).

spread over the ocean to amplify the infragravity waves in deep water.

8. Nearshore Influences

[34] The nearshore region plays three important roles in the long-wave dynamics: (1) alteration of primary-wave-averaged forcing field particularly in the surf zone; (2) edge-trapping of free waves and thereby reduction of their offshore propagation; and (3) resonant amplification when the forcing propagation speed comes close to the phase speed of long waves. We examine the first influence by isolating the forcing in two regions, *i.e.*, in shallow and deep water. To do this two forcing depth scales are introduced, $H_{f\min}$ and $H_{f\max}$. Respectively, these are the minimum and maximum depths where the forcing is applied. The forcing field consists of a periodic alongshore-traveling synoptic storm with a mesoscale modulation (as in section 7). The topography here is an idealized U.S. West Coast topography (Appendix C). The parameterization of primary wave breaking is described in section 5 and Appendix B.

[35] We assume alongshore-homogeneity in the topography by choosing $A_c = 0$, $\lambda_a = \infty$, $h_{\min} = 1$ m, and $h_{\max} = 2600$ m in (C1) in Appendix C. The depth scales $H_{f\max}$ and $H_{f\max}$ are chosen to vary from 20 to 1600 m. A case unconstrained either by $H_{f\max}$ or $H_{f\min}$ is additionally calculated out as the reference case. The long-wave response in Figure 8 shows that the low-frequency and high-frequency free-wave responses are almost identical regardless of $H_{f\max}$, but they depend quite sensitively on $H_{f\min}$. Imposing a finite $H_{f\max}$ is significant only in the high-frequency bound component, although the free component is always larger than the bound component. This implies that the primary-wave forcing in the nearshore region is remarkably important in generation and propagation of long waves throughout the regional oceans. Including $H_{f\max}$ significantly alters the bound $\tilde{\zeta}_{R.M.S.}$ in deep water, which is comparable in magnitude to the free $\tilde{\zeta}_{R.M.S.}$ The results with various $H_{f\min}$ are shown in the three lower panels in Figure 8. The wave responses for both the low-frequency band and high-frequency free components are diminished as $H_{f\min}$ decreases to omit the shallow-water contribution from the forcing field. Removing the shallow-water forcing within only several grid points from the shoreline (*e.g.*, for the case with $H_{f\min} = 20$ m) attenuates $\tilde{\zeta}_{R.M.S.}$ by an order of magnitude compared to the case with no $H_{f\min}$ constraint. However, the wave amplitudes for the low-frequency band converge in the deepest region regardless of $H_{f\min}$. This suggests that the offshore forcing is still responsible for most of the deep-water wave amplitude through the high-frequency

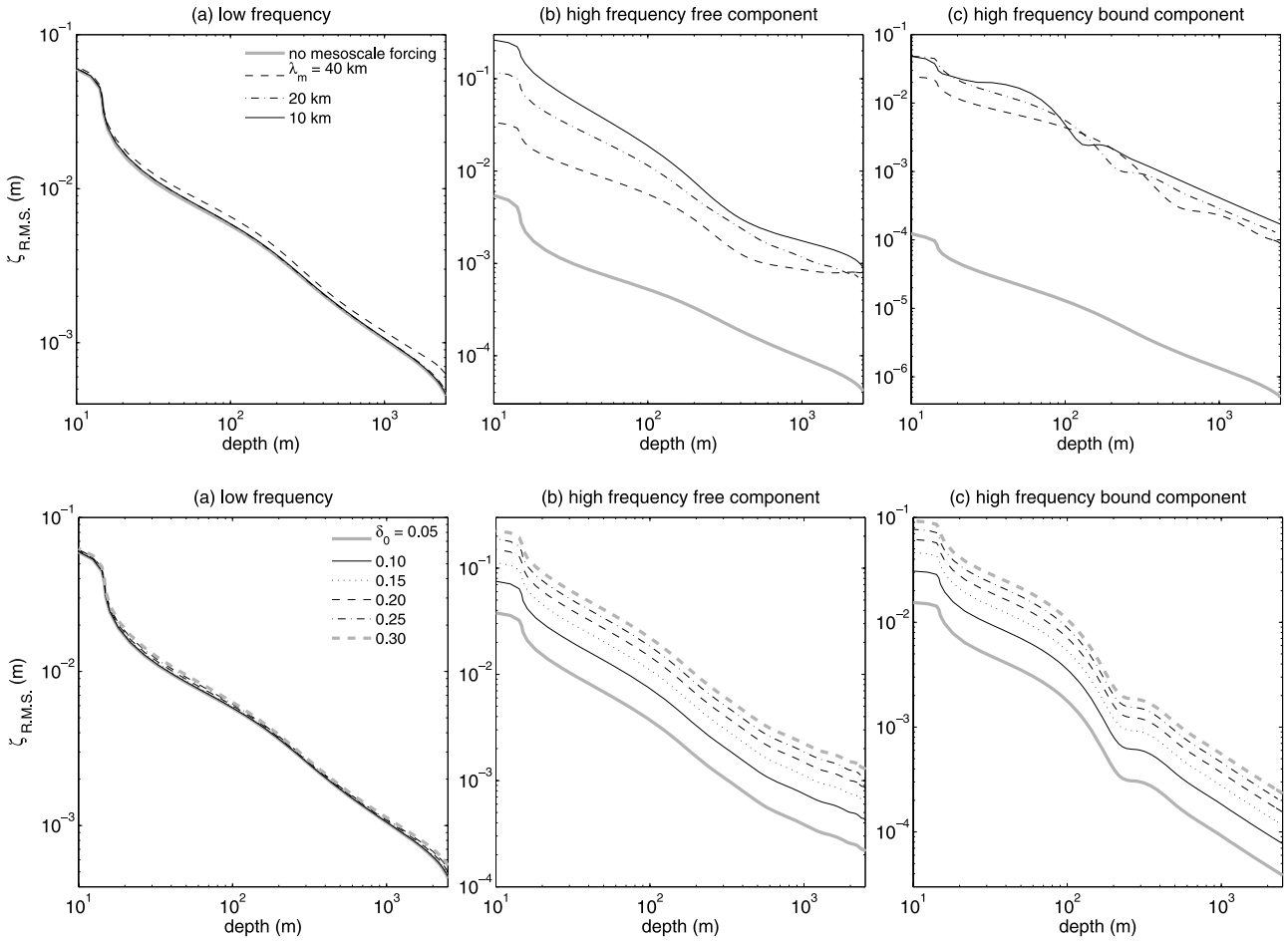

Figure 9. $\tilde{\zeta}_{R.M.S.}$ decomposed for (a) low-frequency band (f < 0.1 mHz), (b) high-frequency free component, and (c) high-frequency bound component for the alongshore-uniform, idealized regional topography: (upper) with mesoscale wavelength λ_m = 10, 20, and 40 km, and with no mesoscale forcing ($\lambda_m = \infty$); (lower) with fractional mesoscale amplitude δ_0 = 0.05, 0.10, 0.15, 0.20, 0.25, and 0.30. Including mesoscale modulation enhances the high-frequency infragravity response.

bound waves. The greater part of the high-frequency free waves here are excited in shallow water and propagate offshore; however, even if the nearshore forcing vanishes, free waves are excited locally in deep water (as also shown in section 7). The free waves generated in deep water propagate shoreward and amplify by the mechanism discussed in section 6.

9. Effects of Mesoscale Forcing Modulation

[36] Inclusion of mesoscale modulation on the synoptic-scale disturbances can cause distinctive enhancement of the wave-averaged forcing $\mathcal{F}$ in mass conservation (3). There are three parameters to determine mesoscale forcing, *viz*., a fractional amplitude δ_0, a phase speed, c^{gr}, and a wave number, $K_m = 2\pi/\lambda_m$, of the mesoscale forcing modulation. Among them, c^{gr} is spontaneously given by the synoptic wavefield as expressed in (22). The other two parameters should be determined through observation or separate estimations of mesoscale forcing development, although *in situ* data on mesoscale waves in deep water is rare. In this section we investigate effects of these two mesoscale parameters on the long-wave response with the present formalism. Regional experiments are conducted on the same topography and synoptic-scale forcing as those used in the preceding section 8, *i.e.*, on the alongshore-uniform idealized U.S. West Coast topography (Appendix C) with the traveling synoptic storm at C_s = 10 m/s in the alongshore direction with mesoscale modulation through λ_m and δ_0. The breaking rule for the primary waves is also introduced as in section 5 and Appendix B. Two types of experiments are performed: (1) various λ_m ranging from 10 to 40 km with a constant δ_0 = 0.16, and (2) various δ_0 ranging from 0.05 to 0.30 with a constant λ_m = 20 km. A case without a mesoscale component is also calculated for reference.

[37] Figure 9 shows the simulated $\tilde{\zeta}_{R.M.S.}$ with various λ_m (upper) and various δ_0 (lower) as a function of depth for (1) low-frequency band, (2) high-frequency free component and (3) high-frequency bound component. Since we imply $\lambda_m < \lambda_s$, inclusion of mesoscale does not influence the low-frequency forcing by the definition in section 4. Hence λ_m and δ_0 do not alter the simulated low-frequency $\tilde{\zeta}_{R.M.S.}$, whereas mesoscale forcing plays a role in altering the high-frequency responses. As indicated in the upper panels, the

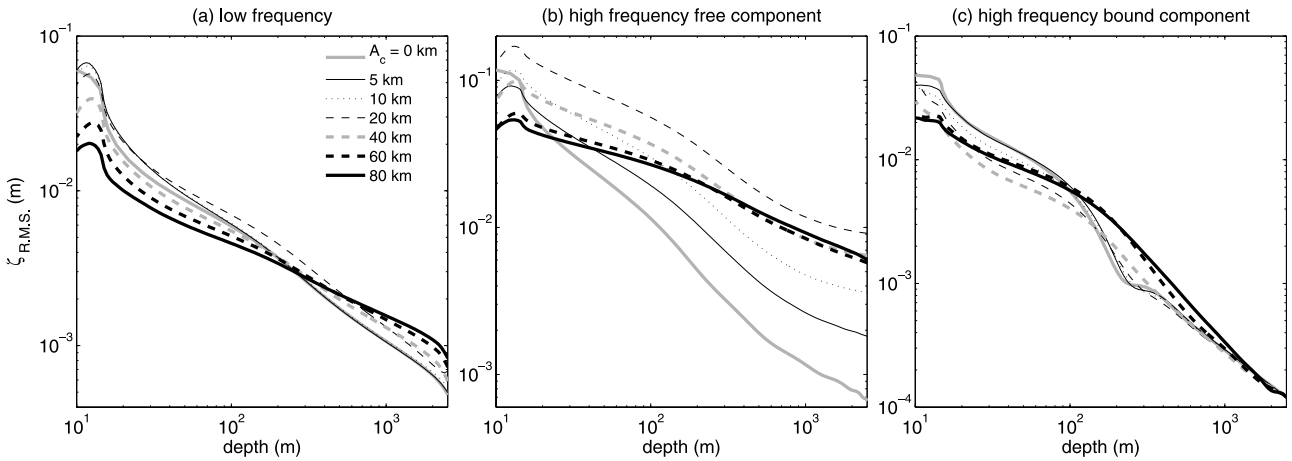

Figure 10. $\tilde{\zeta}_{RM.S.}$ for (a) low-frequency band ($f < 0.1$ mHz), (b) high-frequency bound component, and (c) high-frequency freely propagating component for alongshore-varying topography with various cross-shore topographic amplitudes (A_c = 0, 5, 10, 20, 40, 60 and 80 km) and the standard forcing defined before (39). The alongshore topographic wavelength λ_a is 128 km.

larger K_m (*i.e.*, the smaller λ_m) is, the more energetic are the high-frequency free and bound infragravity waves. The mesoscale forcing,

$$\mathcal{F}_m = -\left[\nabla \mathbf{T}_m^{St} + \frac{\partial \zeta_m^s}{\partial \tau}\right], \tag{35}$$

is approximately proportional to K_m, since the terms proportional to $\nabla(2\delta_m + \delta_m^2)$ and $\partial\tau(2\delta_m + \delta_m^2)$ are dominant in (35). Similarly, the high-frequency $\zeta_{R.M.S.}$ depends on δ_0 as shown in the lower panels in Figure 9. In addition, from (20) with $\Omega_m = K_m c^{gr}$, a larger K_m induces higher-frequency fluctuations in both of forcing and thus response, and of course a larger δ_0 also strengthens the high-frequency wave response.

10. Trapped Modes and Offshore Leakage

[38] Edge waves can be trapped near the shoreline on a sloping planar topography [*e.g.*, *LeBlond and Mysak*, 1978; *Mei*, 1989]. The regional-scale experiments reveals that shallow coastal topographies potentially excites both bound and free infragravity waves owing to a combination of a larger forcing amplitude and resonant amplification (section 6). Ultimately all the infragravity-wave energy may be confined around the shoreline if nearshore bathymetry monotonically deepens into the interior. Suppose the nearshore bathymetry consists of a uniform slope, *viz*., $\tan\beta$ = const., and a straight shoreline with an offshore boundary condition of $\tilde{\zeta} \to 0$ as $x \to \infty$. In such an idealized configuration, *Eckart* [1951] solved the confluent hypergeometric equations derived from the long-wave equation without forcing and found the edge wave dispersion relation corresponding to the following discrete values:

$$\omega_m^2 = gk(2n+1)\tan\beta, \tag{36}$$

where n = 0,1,2,... denotes discretized eigenmode numbers. The associated eigenfunctions are proportional to Laquerre polynomials [*e.g.*, *Mei*, 1989]. *Ursell* [1952] extended this theory to discover the complete edge wave spectrum without the assumption $kh \to 0$ by introducing a wave velocity potential. The resultant discrete edge wave dispersion relation is

$$\omega_n^2 = gk\,\sin[(2n+1)\beta], \tag{37}$$

with $(2n+1)\beta < \pi/2$ and n = 0, 1, 2, ... Equations (36) and (37) indicate that higher modes edge waves tends to propagate further offshore than lower modes. If $\tilde{\zeta}$ has a finite amplitude at $x \to \infty$, then we call this a leaky solution that can exist for

$$\omega^2 > gk. \tag{38}$$

[39] In reality obliquely incident waves and their reflections from the shoreline are refracted on a given sloping topography to form edge waves. However, beyond a certain incident angle, long waves reflected at the shoreline leak offshore and rarely return to the nearshore region. So the leaky mode, as well as higher edge modes, can be responsible for increasing the wave amplitude in deep water.

[40] Edge waves are always found in the present solutions with the sloping topography and shoreline. Given the wave-averaged forcing, the most likely cause that induces offshore propagation of excited infragravity wave is alongshore variability of topography. To assure this we perform computations with A_c = 5, 10, 20, 40, 60, and 80 km (see Figure C1 in Appendix C). We consider two types of forcing. The first one is the same as those imposed in the preceding sections: the alongshore-traveling storm at C_s = 10 m/s and T_s = 6 s with mesoscale amplitude modulation using λ_m = 20 km and δ_0 = 0.16, calling this the standard forcing for convenience. Another type of forcing is also essentially the same as the standard forcing, but the primary wave period T_p on the synoptic storm varies as

$$T_p(X, Y, \tau) = T_m + T_f \cos(K_s Y - \Omega_s \tau). \tag{39}$$

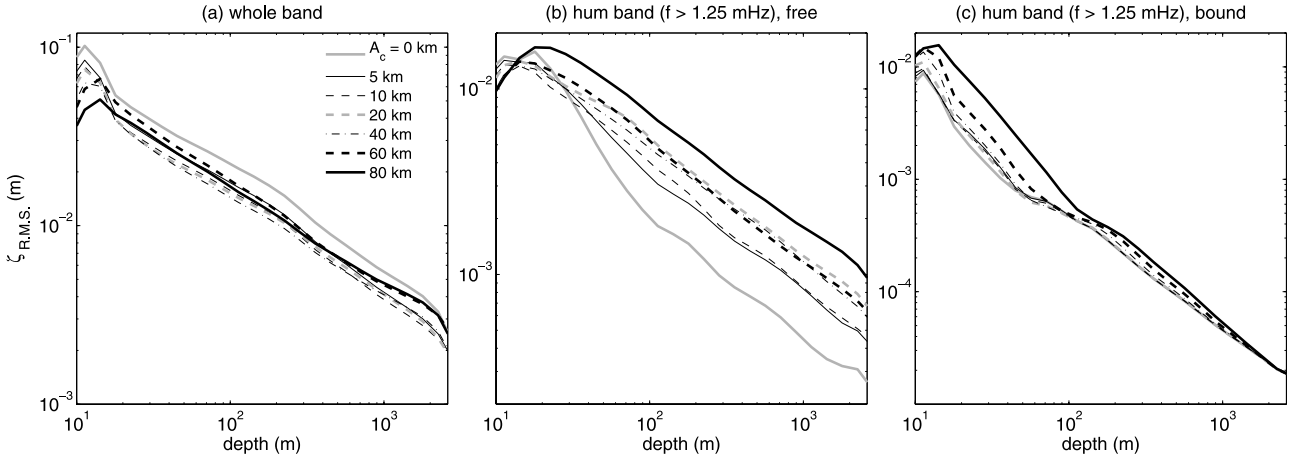

Figure 11. Same as Figure 10 except for using broadband forcing defined after (39) and decomposing $\tilde{\zeta}_{R.M.S.}$ for the hum band ($f > 1.25$ mHz) in Figures (b) and (c).

T_m is a mean period (= 8 s) and T_f is a fluctuating period (= 2 s), so that T_p varies from 6 to 10 s as the synoptic storm evolves. Since dominant frequency of mesoscale forcing is $\Omega_m = K_m\, c^{gr}$ and c^{gr} is altered with T_p, the resultant forcing spectrum becomes much broader than that with the basic forcing. We call this broadband forcing.

[41] Figure 10 shows the decomposed wave responses to the standard forcing with various A_c. As A_c increases $\tilde{\zeta}_{R.M.S.}$ decreases for the low-frequency band, and the high-frequency free component decreases in shallow water but increases in deep water. Consequently, the on-offshore differences in $\tilde{\zeta}_{R.M.S.}$ diminish and make the $\tilde{\zeta}_{R.M.S.}(h)$ curves shallower as the alongshore topographic variability increases (*i.e.*, A_c increases). The high-frequency bound component also changes as the forcing field is altered with A_c, but with a much weaker dependence on A_c than that for the high-frequency free component. Thus the alongshore topographic variability tends to release the offshore wave energy as free waves from the nearshore into deep water, while the bound waves remain concentrated in shallow water. This tendency is also generally true for the cases with the broadband forcing (Figure 11). In particular, on-offshore differences in $\tilde{\zeta}_{R.M.S.}$ in the hum-band free component decrease as A_c increases.

[42] Figure 12 shows the frequency-wave number (reciprocal alongshore wavelength) spectra of the simulated alongshore velocity at 20 m deep for $A_c = 0$ (*viz.*, straight coastline), 5 and 20 km with the broadband forcing. The broken curves illustrate the discrete edge-wave dispersion relation derived by *Ursell* [1952] as represented in (37) on an assumption that the nearshore bottom slope is approximated by $\beta = 0.004$, which is about the mean slope between the shoreline to onshore edge of the shelf break. The solid curves in the low-wave number range are the corresponding leaky cut-off curves defined by (38). The spectra indicate that the infragravity energy tends to concentrate on the discrete, lower mode edge-wave dispersion curves. As A_c increases, the response spectral energy is transferred from the low modes to the higher modes and even to the leaky range. In the straight coastline case (Figure 12 (a)), spectral density is mostly concentrated on the modes 0 and 1 dispersion curves in the region where reciprocal wavelength is negative, coinciding with the incident wave direction. Once alongshore topographic variation is present (*i.e.*, $A_c \neq 0$), spectral energy spreads in the positive reciprocal wavelength. The spectral energy is scattered to high-mode, high-frequency, and low-wave number regions as A_c increases, hence the leaky modes become more significant. These results clearly demonstrate that edge waves are excited most effectively in the straight-coastline case, and the offshore propagation of long waves is less dominant. Alongshore topographic variation acts to transfer the response from the discrete lower edge modes to the higher edge and leaky modes as free waves, reducing $\tilde{\zeta}_{R.M.S.}$ in the nearshore and enhancing it offshore.

11. Basin-Scale Infragravity Waves

[43] *Rhie and Romanowicz* [2004] report strong amplitude for Earth's hum in the North Pacific in a boreal winter. They focus on two distinct hum events between the 31st and 34th Julian days in 2000. The inferred generation site for the hum shifts from the North Pacific to the Southern Ocean between boreal and austral winter. *Rhie and Romanowicz* [2006] further examine these two hum events and detect a lag time of several hours between the seismic signals at their two arrays. Guided by a primary wind-wave analysis with a global wave model, they infer that part of pressure fluctuation in infragravity waves generated by synoptic storms converts to seismic waves locally and propagates long distances as Rayleigh waves to produce the observed hum events at remote sites. The other part is reflected back out into the open ocean as oceanic infragravity wave, propagates across the Pacific basin, and couples to the seafloor near the coast to excite hum remotely. Infragravity waves in the deep ocean and the resulting seismic hum are attributed to a combination of local and remote generation [*Webb et al.*, 1991]; thus, basin-wide simulation is essential. In addition, in the regional simulations in sections 7–10, infragravity waves are most effectively excited near the shore, but they are mostly trapped in shallow water as low-mode edge waves. Alongshore topographic variability can

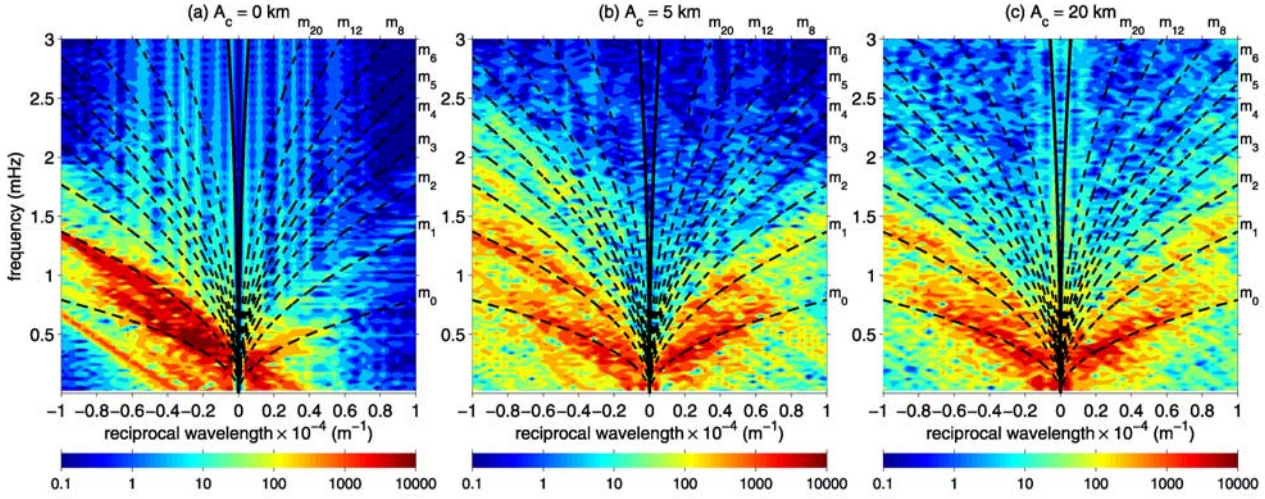

Figure 12. Frequency-wave number (alongshore reciprocal wavelength) spectra of alongshore velocity at $h = 20$ m for three cases with cross-shore amplitude of the alongshore topography (a) $A_c = 0$ (straight coastline), (b) 5 km, and (c) 20 km with alongshore topographic wavelength $\lambda_a = 128$ km. The discrete theoretical edge-wave dispersion curves by *Ursell* [1952] are also plotted by assuming that the nearshore topography is planar with a uniform bottom slope of 0.004. As A_c increases the spectral energy in the low-frequency edge modes spreads over the high-frequency region into both edge modes and leaky modes.

increase the offshore propagation as high-mode edge waves and leaky waves.

[44] To synthesize the influences of these competing processes, realistic basin-scale simulations are necessary to investigate oceanic infragravity waves in relation to global-scale hum generation. We use the forced-dissipative long-wave model in the Pacific Ocean with realistic primary wave-averaged forcing using ECMWF's ERA-40 wave data [*Bidlot et al.*, 2002; *Janssen et al.*, 1997], modulated by mesoscale variability (section 4). The horizontal grid spacing is chosen to be 1/8 °, and the time step is 18 s. For the synoptic scale forcing, statistical wave quantities such as H_s, T_m, θ_m, $\mathbf{T}_s^{St}$and ζ_s^s are computed from the 2D spectral wave data on the ECMWF's analysis grid at a 1.5° resolution and then interpolated on to the model grid with a cubic tension spline interpolation. The nearshore wave number field is modified for $kh < \pi$ as described in section 5 and Appendix B. This modification helps reduce an underestimation of shallow-water infragravity-wave generation in the regional-scale configuration, and it plays a similar role in the Pacific with its even larger grid spacing of 1/8°. On the basis of our experience with different grid spacings, we believe that the residual underestimation bias is not very important for the simulated deep-water response in the Pacific, although almost certainly the simulated nearshore infragravity-wave amplitudes are too small. $\mathcal{F}$ is computed by centered finite differences scheme with second-order accuracy both in space and time. Mesoscale components are evaluated with the parameter values $\lambda_m = 100$ km and $\delta_0 = 0.16$. Since the spatial domain is wider and the length of integration is longer in the basin-scale experiments than those in the regional cases, the effective wave number and frequency due to mesoscale forcing may undesirably become fast-varying functions. To minimize this problem, a piecewise local-origin treatment is implemented to evaluate the phase function of the mesoscale fluctuations as specified in Appendix D.

11.1. Infragravity Waves on 31 January 2000

[45] Basin-scale experiments are made for the first 40 d in 2000 on the 1/8 ° Pacific grid. We first make the calculation as described immediately above, and call this the baseline case. Figure 13 shows sequential snapshots of the long-wave forcing and response fields every 6 h on the 31st day in 2000 for the baseline case. Long waves are observed to spread over the basin and propagate everywhere with a relatively large wavelength compared to the mesoscale wavelength, $\lambda_m = 100$ km. In addition, the simulated $\tilde{\zeta}$ is observed to be generally large near the coasts, in the high latitude regions (*e.g.*, near the Aleutian Arc and along the U.S. West Coast), and in semienclosed bights such as the Yellow Sea, Sea of Japan, South China Sea, and Bering Sea.

[46] The temporal evolution of the long waves is displayed in Figure 14 at several latitudes. Progressive free waves are ubiquitous in all the plots, yet quasi-static responses bound to the forcing appears to be minor. Both easterly and westerly propagations are nearly equally excited with a phase speed approximately equivalent to $\sqrt{gh} \approx 200$ m/s. Long-wave energy is intensified near the coasts probably due to resonant amplification and topographic trapping as examined in sections 6 and 10. The dominant response period in the basin is around 3 h, roughly corresponding to a dominant forcing period of $T_m = \lambda_m / c^{gr} \approx 3$ h. Evolving patterns of long waves are remarkably altered in embayments (*i.e.*, the Yellow Sea in Figure 14b and the Sea of Okhotsk in Figure 14c) from those in the Pacific basin. There is no clear correlation with the generally westerly evolution of the forcing field, indicating a nonresonant response.

[47] Figure 15 shows the R.M.S. wave amplitude averaged over the North Pacific as a function of depth and decomposed into four components: low-frequency ($f \leq 0.1$ mHz); high-frequency free wave ($f > 0.1$ mHz and $c = \Omega/K > 15$ m/s); high-frequency bound wave ($f > 0.1$ mHz and $c \leq 15$ m/s); and hum band ($f > 1.11$ mHz). The high-frequency bound

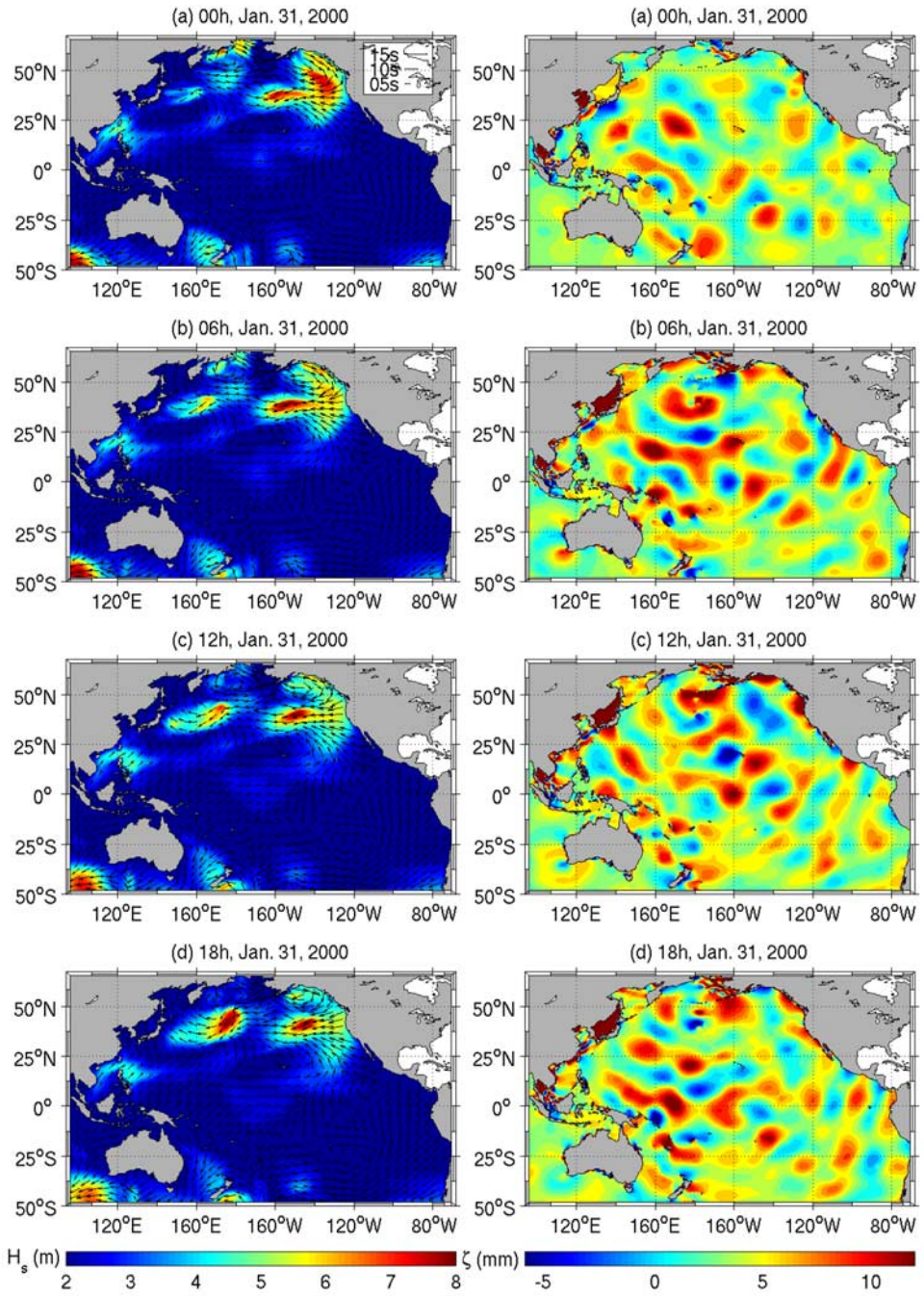

Figure 13. Six-hourly snapshots in the Pacific Ocean of (left) the forcing (the color is the significant wave height H_s in m; the vector direction is mean wave direction θ_m, and the vector length is mean wave period T_m in s), and (right) the wave response field $\tilde{\zeta}$ in mm on 31 January 2000. Freely propagating waves are ubiquitous over the basin, and they do not simply correlate with the forcing.

component decreases more rapidly with depth than the other components; the high-frequency free component has an amplitude of about 2.4×10^{-3} m in shallow water and decreases slowly with depth $\propto h^{-1/4}$ to around 1.0×10^{-3} m in deep water. We attribute the weak depth dependence of $\tilde{\zeta}_{R.M.S.}$ to the complexity of the topography that, which can increase offshore propagation of coastally trapped free waves (section 10), and to the more realistically complex synoptic-scale forcing (plus its associated meso-scale component) in the Pacific that magnifies the deep-water free-wave response. Moreover, the simulated high-frequency amplitude in deep ocean is observed to be approximately consistent with the *in situ* infragravity-wave amplitude reported by *Webb et al.* [1991] in the Pacific Ocean. The high-frequency response is almost equally composed of free and bound waves in shallow water, while free waves dominate over bound waves in deep water. In the baseline case with mesoscale param-

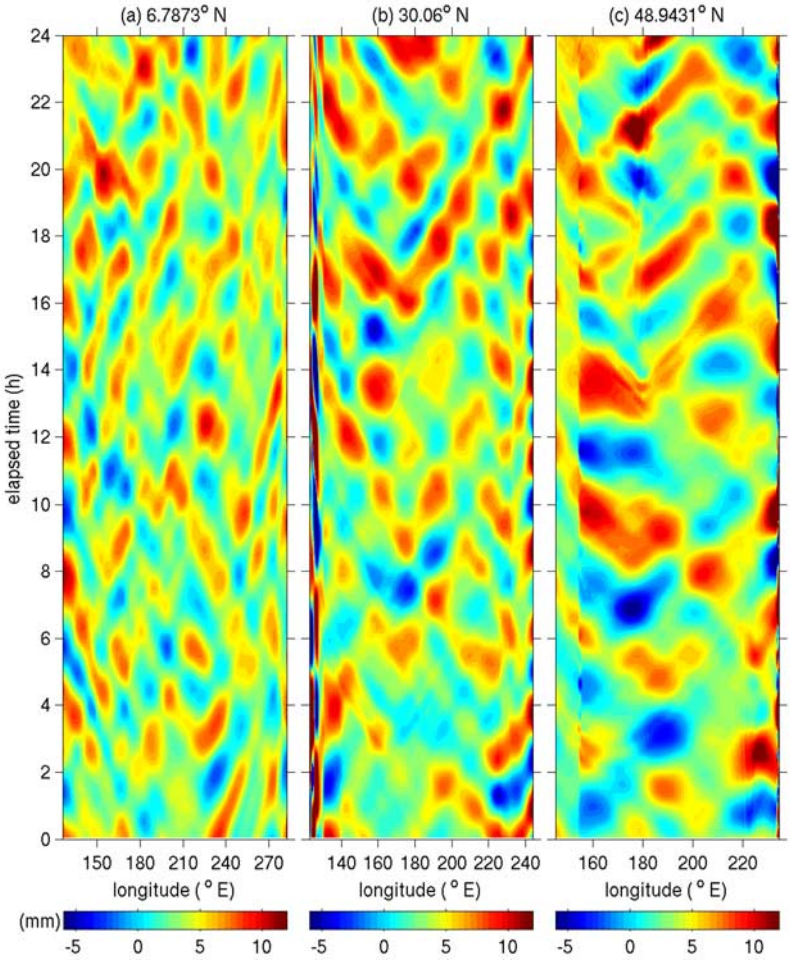

Figure 14. Temporal evolution of $\tilde{\zeta}$ in mm along (a) 6.7873°N, (b) 30.06°N and (c) 48.9431°N on 31 January 2000.

eters λ_m = 100 km and δ_0 = 0.16, $\tilde{\zeta}_{R.M.S.}$ for the hum band is about an order of magnitude smaller than $\tilde{\zeta}_{R.M.S.}$ for the whole high-frequency band.

11.2. Mesoscale and Deep-Water Forcing

[48] The baseline case is now compared to the three types of experiments, *i.e.*, the cases with no offshore forcing, no mesoscale forcing variation, and with higher mesoscale wave numbers (*i.e.*, λ_m = 20, 30, 40, and 60 km). Figure 16 shows the high-frequency component ($f > 0.1$ mHz) for four of these seven cases. Excluding deep-water forcing reduces $\tilde{\zeta}_{R.M.S.}$ to about 30% of the baseline case, especially in deep water. Excluding mesoscale forcing modulation reduces $\tilde{\zeta}_{R.M.S.}$ to merely about 10% of the baseline case. Conversely, increasing K_m boosts $\tilde{\zeta}_{R.M.S.}$ up to almost 10-fold, consistent with section 9 where $\mathcal{F}_m$ and thus the infragravity response are proportional to K_m in (35). While $\zeta_{R.M.S.}$ tends to be intensified near the coasts (*e.g.*, off the U.S. West Coast) for the four cases, it is clear that deep-water forcing is necessary for the long waves to be strong in deep water (*e.g.*, south of the Aleutian Arc where the synoptic-scale forcing is generally intense; Figure 13).

[49] Decomposed $\zeta_{R.M.S.}(h)$ relations are displayed in Figure 17 for all these seven cases. Nearshore responses for the baseline and no offshore forcing cases are almost the same, although offshore amplitude for the baseline case is about 4 times larger than with no offshore forcing. The cases with higher K_m have a larger amplitude for all frequency bands, especially for the hum band. As K_m is higher (λ_m shorter), the long-wave amplitude is larger. The deep-water response is amplified by both nearshore and mesoscale forcing, but it also has a significant component forced in deep water by synoptic storm waves. This latter result is partly in contrast with the regional-scale cases in section 8 with simpler topographies.

[50] The baseline case is further compared to a case with multidirectional mesoscale variations as described in Appendix E, in order to examine importance of directional spreading in mesoscale forcing. It is demonstrated that the multidirectional mesoscale variations do not significantly alter overall amplitudes of the infragravity wave. Therefore the unidirectional, monochromatic representation used throughout the present study is essentially capable of estimating infragravity wave amplitudes without a full spectral consideration of mesoscale modulations.

12. Influence on Earth's Hum

[51] Although infragravity waves have been recognized as a likely cause for seismic hum, it has not been fully understood how large the infragravity amplitude must be to account for observed hum magnitudes. *Tanimoto* [2005]

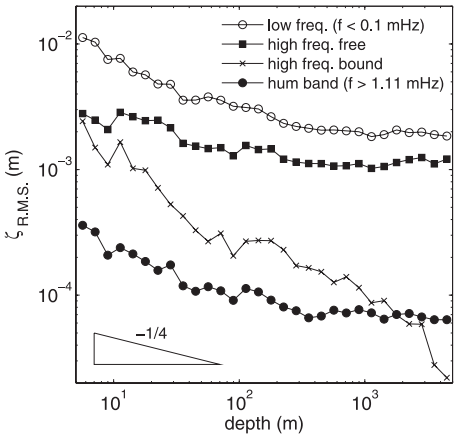

Figure 15. $\tilde{\zeta}_{R.M.S.}$ as a function of depth, averaged over the North Pacific Ocean between 0°N and 56°N and over all 24 h on 31 January 2000. $\tilde{\zeta}_{R.M.S.}$ for the high-frequency ($f > 0.1$ mHz) bound component decreases more rapidly with increasing depth than the other components. The high-frequency free-wave component is around 10^{-3} m in deep water, and its depth dependence is approximately $h^{-1/4}$.

proposes a linear transfer function from stochastic oceanic bottom pressure to seismic vertical acceleration due to normal-mode excitation based on the elastic models of *Tanimoto and Um* [1999] and *Fukao et al.* [2002]. This proposal fits the characteristic shape and level of the low-frequency background noise spectrum, and it indicates that the typical excitation area could be rather small (*i.e.*, about 100×100 km^2) at any given time. It may be controversial [*Rhie and Romanowicz*, 2006; *Webb*, 2007] whether the difference in wavelength between infragravity and elastic waves can be represented by the linear transfer function model; nevertheless, *Tanimoto* [2005] indicates that a bottom pressure spectral density, $< P_b^2 >$, of 10^3 to 10^4 Pa^{2}Hz^{-1} is required for hum generation by infragravity waves.

[52] To check whether our simulations match this requirement, the bottom pressure spectral density, $<P_b^2\ (f)>$, is evaluated from $\tilde{\zeta}$ at four selected locations in the North Pacific (Figure 18) for both the baseline and high K_m (λ_m = 20 km) cases. At low frequencies the long-wave response is much larger than the level required in the hum band. In the baseline case, $<P_b^2\ (f)>$ for the hum band is mostly too small compared to the required amplitude, by about an order of magnitude except in the Bering Sea where $\tilde{\zeta}_{R.M.S.}$ is relatively large (Figure 16a). However, with the larger K_m value (Figure 16), the peak frequency shifts to around 0.5 mHz, and $<P_b^2\ (f)>$ becomes much more energetic in the hum band, ranging from 10^3 to 10^5 Pa^{2}Hz^{-1} in the Bering Sea and off Southern California down to 10^2 to 10^4 Pa^{2}Hz^{-1} west of Hawaii and southeast of Japan. So, with an appropriate mesoscale wave number K_m and fractional amplitude δ_0, the simulated amplitude of the hum-band infragravity waves in the Pacific Ocean is large enough to excite Earth's hum locally both in nearshore shallow water or in the middle of the basin. Of course, our monochromatic model of mesoscale waves is an oversimplification of the broad intermediate, mesoscale band (section 4), and both more field measurements and a more elaborate representa-

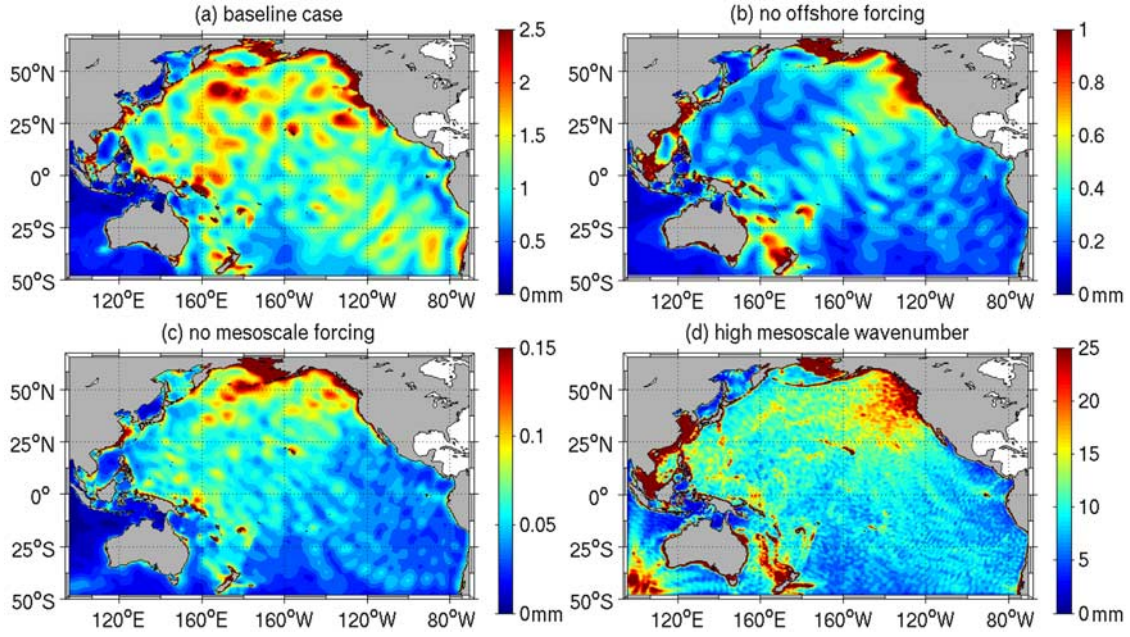

Figure 16. Long-wave response $\tilde{\zeta}_{R.M.S.}$ for the high-frequency component ($f > 0.1$ mHz) on 31 January 2000 for (a) the baseline case; (b) no offshore forcing ($\mathcal{F} = 0$ where $h > 200$ m); (c) no mesoscale forcing ($\delta_0 = 0$); and (d) a higher mesoscale wave number (λ_m = 20 km). Note the different color scales used in each plot. Excluding deep-water and mesoscale forcing significantly reduces $\tilde{\zeta}_{R.M.S.}$, but increasing K_m amplifies it.

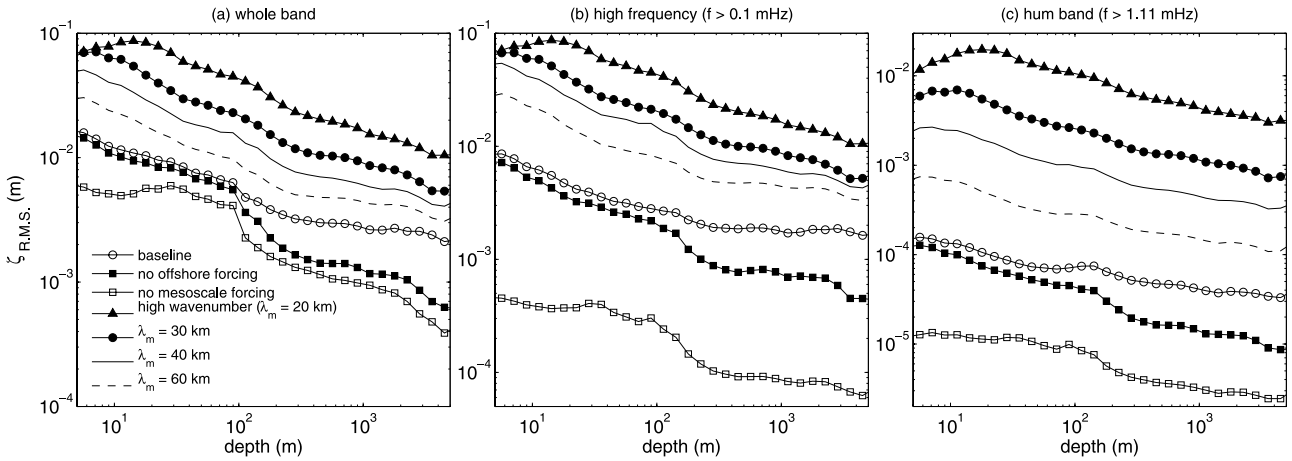

Figure 17. Long-wave response $\tilde{\zeta}_{R.M.S.}$ as a function of depth, averaged over the entire Pacific domain for (a) all frequencies, (b) high-frequencies ($f > 0.1$ mHz), and (c) hum band ($f > 1.11$ mHz) for the four cases in Figure 16. The baseline case has a larger wave amplitude in both shallow and deep water than the cases with no offshore forcing or no mesoscale forcing. Increasing of K_m (*i.e.*, decreasing λ_m from 100 km for the baseline case) remarkably magnifies the response amplitude, especially for the hum band.

tion of the forcing are needed to refine the assessment of hum generation by mesoscale infragravity waves.

13. Conclusions

[53] This paper analyzes the generation and propagation of oceanic infragravity waves as the cause of Earth's continuous background seismic free oscillations, *i.e.*, hum. The dynamics of long gravity waves is modeled by a linearized, forced-dissipative, shallow-water equation and implemented in a 2D version of ROMS. Long-wave forcing is due to quadratic nonlinear interaction among primary wind- and swell-waves on the basis of a multiscale asymptotic wave-current interaction theory. The slowly evolving primary-wave-averaged forcing field is represented by a combination of synoptic-scale variability and mesoscale amplitude modulation. Changes in the primary wave number and wave breaking near the shoreline are based on ray theory and an empirical breaking parameterization.

[54] Resonant amplification is first examined with an analytical solution and 1D, deep-water numerical experiments. The theoretical analysis gives a resonant amplification parameter, $\mathcal{M}_r$ in (29), indicating that an amplified response is expected only in shallow water, while the deep-water response is always off-resonant. From (29) a phase speed of the forcing is found to control amplification of long

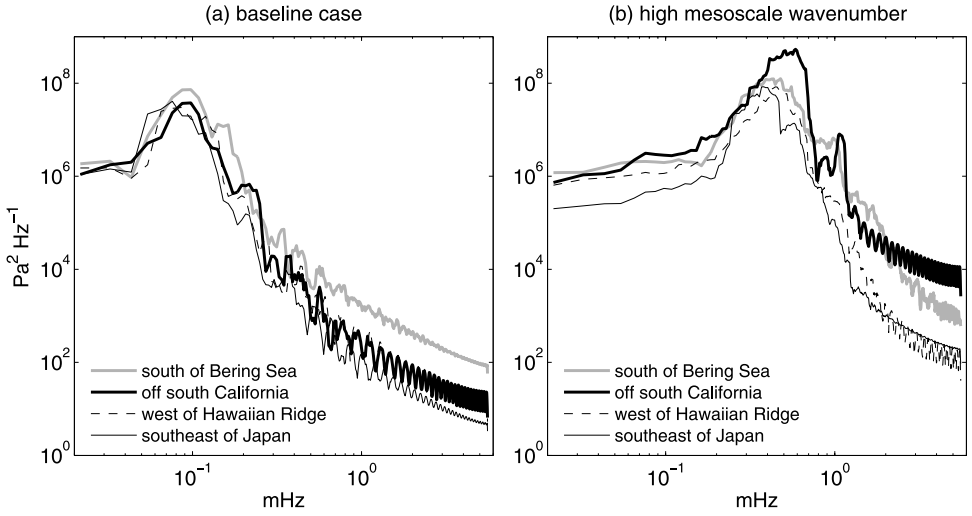

Figure 18. Bottom pressure spectral density, $<P_b^2>$, on 31 January 2000 at four locations in the North Pacific Ocean: south of the Bering Sea (179.20°E, 49.02°N, h = 5140 m); off southern California (122.41°W, 36.37°N, h = 681 m); west of Hawaiian Ridge (152.60°W, 21.72°N, h = 5218 m); and southeast of Japan (137.15°E, 32.28°N, h = 4071 m), for (a) the baseline case and (b) the mesoscale wave number case with λ_m = 20 km. A spectral density greater than about 10^4 Pa^2Hz^{-1} can excite normal-mode seismic oscillations relevant to the observed hum according to the criterion of *Tanimoto* [2005].

waves. A traveling synoptic storm is responsible for low-frequency forcing fluctuations and a bound response, while the speed of mesoscale forcing (*i.e.*, the group speed of the primary waves) more effectively forces high-frequency, freely propagating infragravity waves. Including a solid shoreline amplifies the high-frequency infragravity free waves due to reflection from the shore.

[55] Regional-scale experiments are performed including the shoreline and the depth-induced wave breaking over idealized U.S. West Coast topographies. A baseline case is chosen with an alongshore-uniform topography and a relatively simple forcing by a periodic synoptic storm traveling in the alongshore direction at a constant phase speed, C_s = 10 m/s with a mesoscale amplitude modulation with a fractional amplitude of $\delta_0 = 0.16$ and wavelength of λ_m = 20 km. This forcing excites infragravity waves mostly in shallow water. The infragravity-wave amplitude, $\tilde{\zeta}_{R.M.S.}$ strongly diminishes as the depth increases, approximately inversely proportional to the depth. Contributions in $\tilde{\zeta}_{R.M.S.}$ from free infragravity waves and high-frequency bound waves are nearly unchanged as the depth changes, and free waves are dominant over bound waves everywhere. To investigate the relative contributions of shallow-water and deep-water forcing, we make regional experiments varying the spatial distribution of the primary-wave forcing. Excluding deep-water forcing alters $\tilde{\zeta}_{R.M.S.}$ mainly in the high-frequency bound component in deep water. However, excluding shallow-water forcing significantly diminishes the amplitude at all frequencies for the long-wave response.

[56] The effects of mesoscale forcing variability are represented by two empirical parameters, λ_m and δ_0 in (18) and (19). For simplicity our mesoscale forcing model for λ_m and δ_0 is based on a single mesoscale component and an average fractional amplitude. As λ_m decreases or δ_0 increases, the mesoscale band forcing is amplified. With $\delta_0 \ll 1$ as observed, mesoscale modulation does not affect the low-frequency bound waves, but it is significant for generating high-frequency infragravity waves. Because of (20), λ_m is also significant in determining the frequency of the mesoscale forcing and the high-frequency response amplitude.

[57] Nearshore amplification by edge-trapping and offshore propagation are investigated in the regional-scale configuration. Frequency-alongshore wave number spectra show that freely propagating infragravity waves are refractively trapped near the coast to form edge waves. Horizontal topographic variability is modeled with the cross-shore amplitude of alongshore topographic variability, A_c. As A_c increases offshore propagation of free infragravity waves increases. This offshore propagation occurs as high-mode edge waves and leaky modes. As topographic complexity increases, infragravity energy tends to attenuate in shallow water and magnify in deep water.

[58] Basin-scale infragravity-wave simulations are made for the Pacific Ocean in January and February 2000, to compare to observations of Earth's hum. The simulations demonstrate that free propagation is predominant everywhere in the basin, and the quasi-static response bound to the primary-wave forcing field is secondary. The infragravity-wave response is greater in shallow water and diminishes as the depth increases. Nevertheless, as compared to the idealized regional results, deep-water generation is observed to be more significant in the Pacific because of the complex coastlines that increase offshore propagation (section 10) and the realistic deep-water forcing that can be stronger than the simplified forcing imposed on the regional-scale experiments. With λ_m = 100 km and $\delta_0 = 0.16$, the amplitude of infragravity $\tilde{\zeta}$, integrated over all frequencies, ranges from $O(10^{-3})$ to $O(10^{-2})$ m depending on the depth. If λ_m is decreased to 20 km, the spectral energy of the infragravity waves shifts to a higher frequency band, and the hum band ($f > 1$ mHz) response amplitude increases all over the basin to a level of $O(10^{-2})$ m near the shore and around $O(10^{-3})$ m in deep water. The deep-water amplitude is comparable to the *in situ* amplitude reported by *Webb et al.* [1991], and it is considered to be large enough to excite the hum locally [*Tanimoto*, 2005]. Therefore mesoscale forcing variability in primary wind- and swell-waves probably is responsible for generation of oceanic infragravity waves and the associated seismic hum in both shallow coastal seas and the deep ocean.

Appendix A: Fractional Amplitude δ_0

[59] To obtain Table 1, the synoptic-scale variability of significant wave height H_s (thus amplitude A_s) is evaluated from the ECMWF spectral data on their 1.5° grid with 6 h intervals, using (8) and (A1):

$$A_s(\mathbf{X},\tau) = \frac{1}{2}H_s(\mathbf{X},\tau) = 2\sqrt{\overline{\eta_p^2}}. \tag{A1}$$

[60] Then bilinear interpolation both in time and space is performed to compute A_s at each data point corresponding to the TOPEX satellite data,

$$A_s(\mathbf{X},\tau) \rightarrow A_s(X_T,\tau_T), \tag{A2}$$

where X_T and τ_T are the along-satellite-path spatial coordinate and time of the measurement. With $A_s(X_T, \tau_T)$ from the ECMWF data and its counterpart, *i.e.*, $A_T(X_T, \tau_T)$ directly obtained from the TOPEX data set, the wave number spectra $P_s(k)$ and $P_T(k)$ are estimated. From the definition,

$$\overline{A_s^2} = \int_0^{k_s} P_s(k)dk; \quad \overline{A_T^2} = \int_0^{kT} P_T(k)dk, \tag{A3}$$

where k_s and k_T are the cut-off wave numbers,

$$k_s = 2\pi/L_s; \quad k_T = 2\pi/L_T, \tag{A4}$$

with L_s and L_T ($L_s > L_T$, hence $k_s < k_T$) the spatial intervals of the ECMWF and TOPEX wave data. The mesoscale variance of wave amplitude, $\overline{A_m^2}$, is then expressed as

$$\overline{A_m^2} = \int_{k_s}^{k_T} P_T(k)dk, \tag{A5}$$

since we define the cut-off wave number for the mesoscale variations to be k_s (section 4). Consequently, δ_0 can be evaluated by (23). A similar procedure has been applied for the NDBC data (Table 2) with the cut-off frequency of the wave amplitude spectra computed from the ECMWF data at

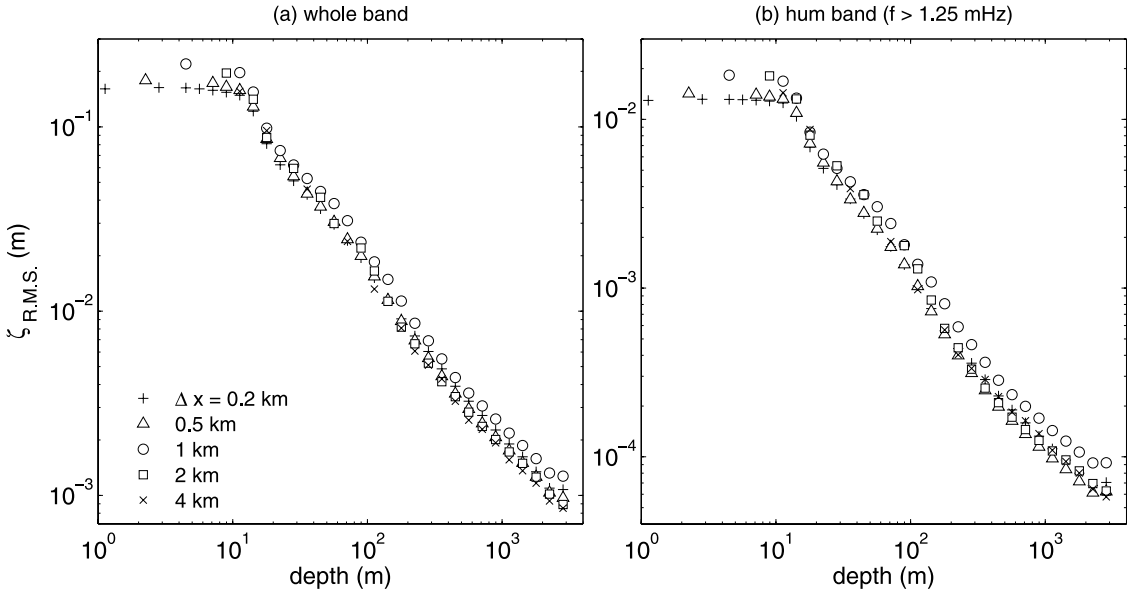

Figure B1. Long-wave responses with various grid spacings with ΔX = 0.2, 0.5, 1, 2, and 4 km for (a) the whole band and (b) the hum band (f > 1.25 mHz) on an idealized regional domain without alongshore topographic variability. The mesoscale forcing is configured with λ_m = 20 km.

each buoy locations as the cut-off frequency for the mesoscale amplitude variance.

Appendix B: Discrete Evaluation of Nearshore Wave Parameterization

[61] In regional and basin-scale configurations with a large grid-spacing $\approx 10^3$ to 10^4 m, the surf zone may be represented by a single grid cell next to the shore, although the primary wavefield could change substantially within the cell due to shoaling, refraction and breaking. So we can include subgrid-scale variability into $\mathcal{F}$. First, to avoid singularity in wave amplitude A as $h \to 0$, a smoothing operator for A is introduced.

$$A(h) = \left[\frac{\left(\frac{1}{2}\gamma h\right)^m}{1 + \left\{ \frac{1}{2}\gamma h \sqrt{\left(c_g k_\perp \mathcal{P}_\infty\right)^{-1} |\mathbf{k}|} \right\}^m} \right]^{1/m} . \qquad \text{(B1)}$$

$\mathcal{P}_\infty$ is constant along a wave ray in (26) at an arbitrary offshore location where the primary wave amplitude, period and direction and the local depth are all known. m is an *ad hoc* blending parameter that controls smoothness around breaking point. Here m = 8 is chosen to attain a sufficiently smooth change in A in the vicinity of breaking point. A grid-

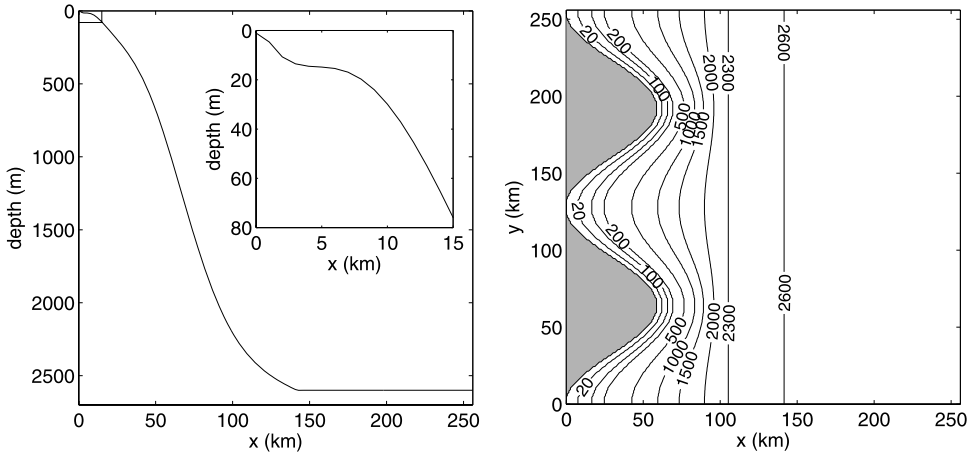

Figure C1. Left: depth profile of the idealized regional bathymetry in (C1) at y = 0 km with $h_{\min}$ = 1 m, A_c = 60 km, λ_a = 128 km, and x_c = 140 km. The inset is a blow-up of the nearshore region. Right: a plan view of the isobaths in m.

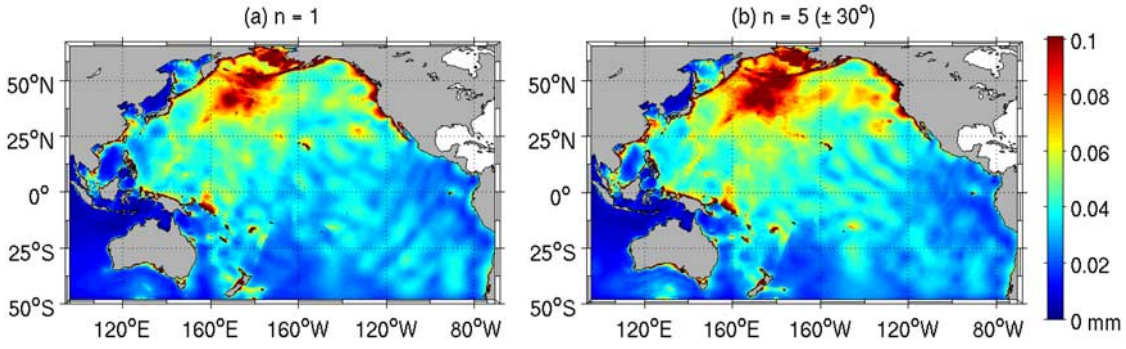

Figure E1. Long-wave response $\tilde{\zeta}_{R.M.S.}$ for the hum-band component ($f > 1.11$ mHz) on 31 January 2000 for (a) the baseline case ($n = 1$); and (b) $n = 5$ (±30 deg.). Inclusion of multidirectional mesoscale components provide slightly more variability in $\tilde{\zeta}_{R.M.S.}$ for each frequency band than the baseline case.

averaging operator is subsequently introduced for $\mathcal{F}$, as well as for (25), (B1), and the dispersion relation (2):

$$\begin{aligned}\bar{\mathcal{F}} &= -\overline{\nabla\cdot\mathbf{T}^{St}} - \frac{\overline{\partial\zeta^{s}}}{\partial\tau},\\ &\approx -\frac{1}{\Delta h}\int_{h_b}^{h_a}\nabla\left(\frac{gA(h)^2}{2\,c(h)}\frac{\mathbf{k}(h)}{k(h)}\right)dh\\ &\quad -\frac{\partial}{\partial\tau}\left\{\frac{1}{\Delta h}\int_{h_b}^{h_a}\frac{A(h)^2}{2h}\left(\frac{c_g(h)}{c(h)}-\frac{1}{2}\right)dh\right\},\\ &\approx -\frac{g}{2\Delta h}\tan\beta_X\left(\frac{A^2k_X}{ck}\bigg|_{h_a}-\frac{A^2k_X}{ck}\bigg|_{h_b}\right)\\ &\quad -\frac{g}{2\Delta h}\tan\beta_Y\left(\frac{A^2k_Y}{ck}\bigg|_{h_a}-\frac{A^2k_Y}{ck}\bigg|_{h_b}\right)\\ &\quad -\frac{\partial}{\partial\tau}\left[\frac{1}{2N}\sum_{n=1}^{N}\frac{A^2(h_n)}{h_n}\left\{\frac{c_g(h_n)}{c(h_n)}-\frac{1}{2}\right\}\right].\end{aligned} \tag{B2}$$

[62] The overbar $\bar{\cdot}$ denotes the grid-averaging operator; h_a and h_b are the deepest and shallowest water depths in the single grid cell of interest; $\Delta h = h_a - h_b$, $\tan\beta_X$ and $\tan\beta_Y$ are the constant bottom slopes of the cell in the two horizontal directions; (k_X, k_Y) is the horizontal wave number vector; and $h_n = h_b + \frac{n}{N}\Delta h$ is a discretized depth in which $n = 0, 1, 2, \cdots, N$ and $h_b \le h_n \le h_a$. We set N to be 50 for a sufficient resolution of the changes in the primary wavefield in the nearshore area. In practice, the grid-averaging is applied for the primary wavefield in the shallow water where $kh < \pi$ ($h/L < 0.5$) since the forcing term significantly varies only in this range. Otherwise, a simple centered finite difference scheme is adopted for the both terms in $\mathcal{F}$ using the primary-wave quantities and the local depth at the cell center.

[63] With this approach we are able to investigate generation and propagation of deep-ocean infragravity long-waves with a relatively large grid spacing, which in practice enables us to conduct large-region and basin-scale, phase-resolved, infragravity wave simulations (Figure B1). As a practical matter, one cannot simultaneously pursue a detailed resolution of the nearshore region and do broad-area depiction of the hum-forcing long waves. We believe we have done a sufficiently good job with the former in order to be able to adequately address the latter.

Appendix C: Regional Configuration

[64] We specify an idealized coastal topography by taking am alongshore-average of the U.S. West Coast topography

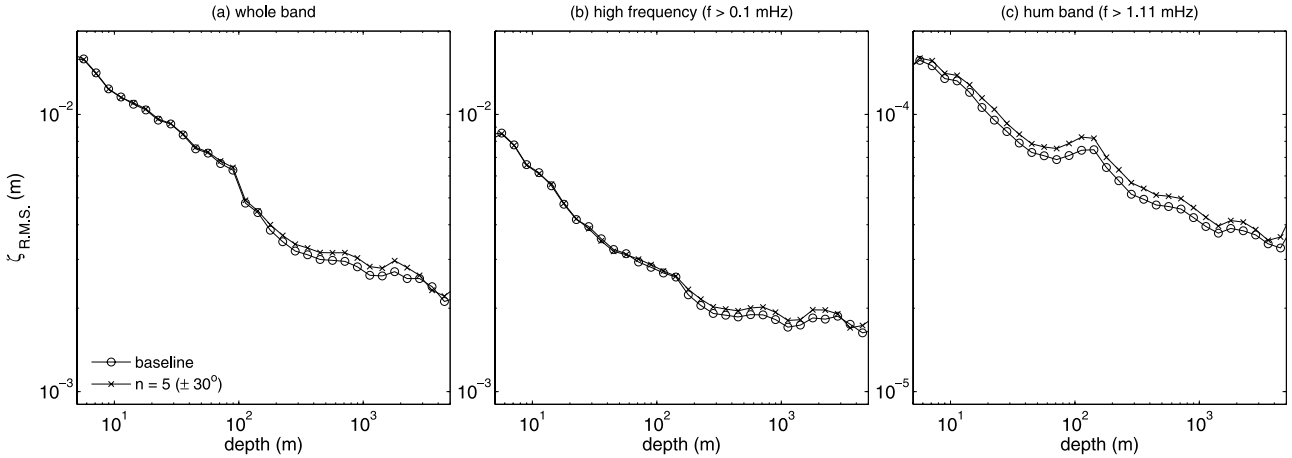

Figure E2. Long-wave response $\tilde{\zeta}_{R.M.S.}$ as a function of depth, averaged over the entire Pacific domain for (a) all frequencies, (b) high-frequencies ($f > 0.1$ mHz), and (c) hum band ($f > 1.11$ mHz) for the two cases in Figure E1.

between about 40.6 and 48.2°N (off the Oregon Coast). The resulting idealized topography is approximated by the following equations:

$$
\begin{aligned}
x_s(y) &= \frac{A_c}{2}\left\{1-\cos\left(\frac{2\pi}{\lambda_a}y\right)\right\}\\
x_m(y) &= \max\left[x, x_c\frac{x-x_s(y)}{x_c-x_s(y)}\right]\\
h(x,y) &= a_0 x_m \tanh(b_1 x_m) + d_1\{1-\exp(a_1 x_m)\}\\
&\quad - d_2\exp\left\{-a_2\left(\frac{x_m-x_p}{x_p}\right)^2\right\}\tanh(b_2 x_m)\\
h(x,y) &= \max[h_{\min}, \min\{h(x,y), h_{\max}\}].
\end{aligned}
\tag{C1}
$$

x ($\geq$0) is distance cross-shore; y is the alongshore coordinate; $x_s(y)$ is shoreline position from $x = 0$; x_m is a shrunk cross-shore coordinate modified by x_s and x_c; x_c is the offshore distance beyond which the topography is uniform alongshore; A_c is a cross-shore amplitude of sinusoidal shoreline topography; λ_a is the alongshore wavelength of the sinusoidal shoreline; $d_1 = 2850.0$ m is the maximum offshore depth; $d_2 = 970.0$ m is the peak depth at the shelf break; $x_p = 4.3 \times 10^4$ m is offshore distance to the shelf peak; $a_0 = 0.9 \times 10^{-3}$ is a nearshore bottom slope; $a_1 = -1.7 \times 10^{-5}$ and $a_2 = 1.2$ are cross−shore spreading parameters; and $b_1 = 5.0 \times 10^{-7}$ and $b_2 = 1.3 \times 10^{-4}$ are attenuation parameters to reduce the topographic variability in a far field. The bathymetry is further constrained by $h_{\min}$ and $h_{\max}$, the minimum and maximum water depths in the domain.

[65] An example of the idealized topography is illustrated in Figure C1. The topography has a foreshore steep slope in the vicinity of the shoreline defined at $x = 0$ to about a few kilometers offshore as shown in the cross-sectional depth profile (left panel), followed by a relatively mild continental shelf extending for about several kilometers where the depth ranges around 16 m. Afterward, a steeper shelf break emerges to increase the depth down to 2600 m, and then a flat bathymetry appears in the deep offshore area of $x > x_c = 140$ km. Alongshore variability is controlled by parameters A_c and λ_a. In the right panel, $A_c = 60$ km and $\lambda_a = 128$ km are assigned.

[66] In the regional-scale computations discussed in sections 8–10, a periodic lateral boundary condition in the Y-direction and a Flather-type inflow open boundary condition in the X-direction at the offshore boundary ($X = 256$ km) are applied. Grid spacings in the both horizontal directions are constant: $\Delta X = \Delta Y = 1$ km. A time step of $\Delta\tau = 3.2$ s is set by the computational-stability criterion.

Appendix D: A Local Origin for Mesoscale Variability

[67] We specified a representation for the primary wave amplitude that includes both the synoptic-scale variations and a mesoscale component as expressed by equations (16) and (19) in section 4,

$$A(\mathbf{X},\tau) = A_s(1+\delta_0\sin\Theta), \tag{D1}$$

where $\delta_0 < 1$ and

$$
\begin{aligned}
\Theta &= K_m(\cos\theta_p X + \sin\theta_p Y) - K_m c_g(\mathbf{X},\tau)\tau\\
&\equiv k_m X + \ell_m Y - \Omega_m \tau
\end{aligned}
\tag{D2}
$$

is a phase function. The variables with subscript s vary on the synoptic scale in space and time and are determined from the ECMWF wave analysis. The quantities $K_m = \sqrt{k_m^2+\ell_m^2}$ and δ_0 are constants associated with the mesoscale modulation. K_m^{-1} is assumed to be much smaller than the synoptic scale. Thus the mesoscale wave numbers and frequency (k_m, ℓ_m, and Ω_m) are also slowly varying functions.

[68] Our challenge is to evaluate (D1) and obtain a result that has oscillations only near the mesoscale wave numbers and frequency that are slowly varying. A straightforward evaluation of Θ in (D2) does not meet this criterion. This can be illustrated with a 1D example:

$$F(\xi) = \sin\hat{\Theta}, \qquad \hat{\Theta} = k(\xi)\xi. \tag{D3}$$

The effective wave number for this function is

$$\frac{\partial\hat{\Theta}}{\partial\xi} = k + \xi\frac{\partial k}{\partial\xi}. \tag{D4}$$

Even if $\partial_\xi k$ is small (*i.e.*, k is slowly varying), ξ can be arbitrarily large, and the effective wave number can be very different from k, either much larger or smaller.

[69] A remedy for this bad behavior is to replace the sinΘ function with piecewise constant wave numbers and frequency. For (D1), the first step is to expand the oscillatory function into separate coordinate function factors,

$$
\begin{aligned}
\sin\Theta &= \sin[k_m X]\cos[\ell_m Y]\cos[\omega_m T]\\
&\quad + \sin[k_m X]\sin[\ell_m Y]\sin[\omega_m T]\\
&\quad + \cos[k_m X]\sin[\ell_m Y]\cos[\omega_m T]\\
&\quad - \cos[k_m X]\cos[\ell_m Y]\sin[\omega_m T].
\end{aligned}
\tag{D5}
$$

If each of these 6 right-side functions can be appropriately represented, then the total function will be.

[70] We can illustrate an appropriate representation using the illustrative function (D3). First consider a piecewise constant approximation where F is continuous between ξ intervals but has a discontinuous derivative (*i.e.*, is a C^0 function). First define intervals in ξ of size $\Delta\xi$:

$$\xi_{n+1} = \xi_n + \Delta\xi, \qquad \xi_0 = 0, \qquad \xi_{n+0.5} = \xi_n + 0.5\cdot\Delta\xi. \tag{D6}$$

Within each interval, $\xi_n \leq \xi \leq \xi_{n+1}$, $k(\xi)$ is held constant at a value of $k_{n+0.5} = k(\xi_{n+0.5})$. This means that the second term in (D4) is missing and that the oscillations in F in (D3) will have a wave number that is the local value of k. The function itself is approximated by

$$
\begin{aligned}
&F_{0.5}(\xi) = \sin[k_{0.5}\xi], \qquad \xi_0 \leq \xi \leq \xi_1,\\
&F_1 = F_{0.5}(\xi) = \sin[k_{0.5}\Delta\xi].
\end{aligned}
\tag{D7}
$$

$$
\begin{aligned}
&F_{1.5}(\xi) = F_1 + \sin[k_{1.5}(\xi-\Delta\xi)], \qquad \xi_1 \leq \xi \leq \xi_2,\\
&F_2 = F_{1.5}(\xi_2) = F_1 + \sin[k_{1.5}\Delta\xi].\\
&\quad\cdots
\end{aligned}
$$

$$F_{n+0.5}(\xi) = F_n + \sin[k_{n+0.5}(\xi - n\Delta\xi)],$$
$$\xi_n \le \xi \le \xi_{n+1},\ F_{n+1} = F_{n+0.5}(\xi_{n+1}) = F_n + \sin[k_{n+0.5}\Delta\xi]. \quad \text{(D8)}$$

Note that this can be made into a $\mathcal{C}^1$ function by doing weighted averaging across the interval boundary: *i.e.*, in $\xi_n - \mu\Delta\xi/2 \le \xi \le \xi_n + \mu\Delta\xi/2$,

$$\tilde{F}_n(\xi) = \left\{1 - (\mu\Delta\xi)^{-1}[\xi - \xi_n + \mu\Delta\xi/2]\right\}F_{n-0.5}(\xi) + (\mu\Delta\xi)^{-1}[\xi - \xi_n + \mu\Delta\xi/2]F_{n+0.5}(\xi). \quad \text{(D9)}$$

We choose $\mu = 1$ for computational efficiency, avoiding overlap between the averaging intervals. In the basin-scale experiments in section 11, $\delta\xi = 500$ when the mesoscale wavelength λ_m ranges between 20 and 100 km.

Appendix E: Multidirectional Mesoscale Variations

[71] The mesoscale variations partially includes the familiar "group" modulations at typical scales of several primary wavelengths. This second-order low frequency modulation is intrinsically more broadbanded in direction than the primary wave trains [*e.g.*, *Hasselmann*, 1962]. Hence the unidirectional monochromatic approach taken in the present study might be a bit too crude, provided that the group modulations are predominant in the mesoscale variations. We thus test the mesoscale forcing from this perspective by introducing directional spreading through linear superposition of multiple mesoscale components distributed around the spectral-peak primary wave direction, θ_p. Therefore equations (19) and (21) are modified as

$$\delta_m(\mathbf{X}, \tau) = \sum_n \delta_n \sin[\mathbf{K}_n \cdot \mathbf{X} - \Omega_m \tau], \quad \text{(E1)}$$

$$\mathbf{K}_n(\mathbf{X}, \tau) = [K_m \cos\theta_n,\ K_m \sin\theta_n]. \quad \text{(E2)}$$

where $\mathbf{K}_n$, δ_n and θ_n are an n-th mesoscale wave number vector, an n-th fractional amplitude, and a propagating direction of the n-th mesoscale component (arbitrary angular distribution function), respectively. δ_n is simply determined to conserve of the total mesoscale wave-height variance,

$$\delta_n^2 = \delta_0^2 P_n \ ;\ \sum_n P_n = 1 \quad \text{(E3)}$$

where P is an arbitrary probability density function.

[72] We show a result with five mesoscale components, *i.e.,* $n = 5$, $P_n = (0.05, 0.15, 0.6, 0.15, 0.05)$, $\theta_n - \theta_p = (-30°, -15°, 0°, 15°, 30°)$ and $\lambda_m = 100$ km so as to compare with the baseline case (section 11). $\zeta_{R.M.S.}$ for the hum band (Figure E1) illustrates that spatial patterns and magnitude of $\zeta_{R.M.S.}$ are almost the same for the two cases whereas there is slightly more spatial spreading with $n = 5$ than $n = 1$. Spatially averaged $\tilde{\zeta}_{R.M.S.}$ (Figure E2) also shows that the multidirectional mesoscale variability does not play a substantial role in modifying the overall amplitude of the long-wave response. We have conducted a few more tests with different choices of P_n and θ_n, and obtained essentially similar results. The spectrum-peak primary wave direction, $\theta_p(\mathbf{X}, \tau)$, is complicatedly distributed throughout the basin and changes with time (Figure 13) in response to the synoptic-scale wavefield. In addition the resultant infragravity waves that mostly propagate as free waves readily become broadbanded in direction through refraction on the complex bathymetry and reflection from the shoreline. Hence the simple, unidirectional, monochromatic mesoscale amplitude expression ($n = 1$) instigates considerable directional variability in practice, which allows us to estimate infragravity wave amplitudes without making a full spectral consideration of the mesoscale modulations.

[73] **Acknowledgments.** This study was financially supported by the Office of Naval Research with grant N00014-04-1-0166. The authors are grateful to A. F. Shchepetkin (UCLA) for his support of the development of the long-wave model based on ROMS. We also wish to express appreciation to P.A.E.M. Janssen and J.-R. Bidlot (ECMWF) and E. Huckle (UCLA) for help with processing the ERA40 global wave data.

References

Battjes, J. A. (1972), Radiation stresses in short-crested waves, *J. Mar. Res.*, *30*, 56–64.

Battjes, J. A., and M. J. F. Stive (1985), Calibration and verification of a dissipation model for random breaking waves, *J. Geophys. Res.*, *90*(C5), 9159–9167.

Bidlot, J.-R., D. J. Holmes, P. A. Wittmann, R. Lalbeharry, and H. S. Chen (2002), Intercomparison of the performance of operational ocean wave forecasting systems with buoy data, *J. Phys. Oceanogr.*, *17*, 287–310.

Bowen, A. J., and R. T. Guza (1978), Edge waves and surf beat, *J. Geophys. Res.*, *83*(C4), 1913–1920.

Callahan, P. S., C. S. Morris, and S. V. Hsiao (1994), Comparison of topex/poseidon σ_0 and significant wave height distributions to geosat, *J. Geophys. Res.*, *99*(C12), 25,015–25,024.

Eckart, C. (1951), Surface waves on water of variable depth, in *Wave Rep.*, *100*, 99 pp., Scripps Inst. of Oceanogr., La Jolla, Calif.

Ekström, G. (2001), Time domain analysis of Earth's long-period background seismic radiation, *J. Geophys. Res.*, *106*(B11), 26,483–26,493.

Foda, M. A., and C. C. Mei (1981), Nonlinear excitation of long-trapped waves by a group of short swells, *J. Fluid Mech.*, *111*, 319–345.

Fukao, Y., K. Nishida, N. Suda, K. Nawa, and N. Kobayashi (2002), A theory of the earth's background free oscillations, *J. Geophys. Res.*, *107*(B9), 2206, doi:10.1029/2001JB000153.

Gallagher, B. (1971), Generation of surf beat by non-linear wave interactions, *J. Fluid Mech.*, *49*, 1–20.

Guza, R. T., and E. B. Thornton (1982), Swash oscillations on a natural beach, *J. Geophys. Res.*, *87*(C1), 483–492.

Hasselmann, K. (1962), On the non-linear energy transfer in a gravity-wave spectrum. part I: General theory, *J. Fluid Mech.*, *12*, 481–500.

Hasselmann, K. (1963), A statistical analysis of the generation of microseisms, *Rev. Geophys.*, *1*(2), 177–209.

Herbers, T. H. C., S. Elgar, and R. T. Guza (1994), Infragravity-frequency (0.005–0.05 hz) motions on the shelf. part I: Forced waves, *J. Phys. Oceanogr.*, *24*, 917–927.

Herbers, T. H. C., S. Elgar, R. T. Guza, and W. C. O'Reilly (1995a), Infragravity-frequency (0.005–0.05 hz) motions on the shelf. part II: Free waves, *J. Phys. Oceanogr.*, *25*, 1063–1079.

Herbers, T. H. C., S. Elgar, and R. T. Guza (1995b), Generation and propagation of infragravity waves, *J. Geophys. Res.*, *100*(C12), 24,863–24,872.

Huntley, D. A., R. T. Guza, and E. B. Thornton (1981), Field observations of surf beat: 1. Progressive edge waves, *J. Geophys. Res.*, *86*(C7), 6451–6466.

Janssen, P. A. E. M., B. Hansen, and J.-R. Bidlot (1997), Verification of the ECMWF wave forecasting system against buoys and altimeter data, *J. Phys. Oceanogr.*, *12*, 763–784.

Kenyon, K. E. (1969), Stokes drift for random gravity waves, *J. Geophys. Res.*, *74*(28), 6991–6994.

Kenyon, K. E. (1970), Stokes transport, *J. Geophys. Res.*, *75*(06), 1133–1135.

Kobayashi, N., and K. Nishida (1998), Continuous excitation of planetary free oscillations by atmospheric disturbances, *Nature*, *395*, 357–360.

Komen, G. J., L. Cavaleri, M. Donelan, K. Hasselmann, S. Hasselmann, and P. A. E. M. Janssen (1994), *Dynamics and Modelling of Ocean Waves*, Cambridge Univ. Press, Cambridge, UK.

LeBlond, P. H. and L. A. Mysak (1978), *Waves in the Ocean*, Elsevier, Amsterdam, Netherlands.

Lighthill, J. (1978), *Waves in Fluids*, Cambridge Univ. Press, Cambridge, UK.

Longuet-Higgins, S. (1950), A theory of the origin of microseisms, *Philos. Trans. R. Soc. London, Ser. A*, *243*, 1–35.

Longuet-Higgins, M. S., and R. W. Stewart (1962), Radiation stress and mass transport in gravity waves, with application to "surf beats", *J. Fluid Mech.*, *13*, 481–504.

McWilliams, J. C., J. M. Restrepo, and E. M. Lane (2004), An asymptotic theory for the interaction of waves and currents in coastal waters, *J. Fluid Mech.*, *511*, 135–178.

Mei, C. C. (1989), *The Applied Dynamics of Ocean Surface Waves*, World Scientific, Singapore.

Munk, W. H. (1949), Surf beat, *Eos Trans. AGU*, *30*, 849–854.

Munk, W. H., F. E. Snodgrass, and F. Gilbert (1964), Long waves on the continental shelf: An experiment to separate trapped and leaky modes, *J. Fluid Mech.*, *20*, 529–554.

Nawa, K., N. Suda, Y. Fukao, T. Sato, Y. Aoyama, and K. Shibuya (1998), Incessant excitation of the earth's free oscillations, *Earth Planets Space*, *50*, 3–8.

Nieto Borge, J. C., S. Lehner, A. Niedermeier, and J. Schulz-Stellenfleth (2004), Detection of ocean wave groupiness from spaceborne synthetic aperture radar, *J. Geophys. Res.*, *109*, C07005, doi:10.1029/2004JC002298.

Nishida, K., N. Kobayashi, and Y. Fukao (2000), Resonant oscillations between the solid earth and the atmosphere, *Science*, *287*, doi:10.1126/science.287.5461.2244.

Okihiro, M., R. T. Guza, and R. J. Seymour (1992), Bound infragravity waves, *J. Geophys. Res.*, *97*(C7), 11,453–11,469.

Oltman-Shay, J., and R. T. Guza (1987), Infragravity edge wave observations on two California beaches, *J. Phys. Oceanogr.*, *17*, 644–663.

Proudman, J. (1953), *Dynamical Oceanography*, Methuen, London, UK.

Rhie, J., and B. Romanowicz (2004), Excitation of Earth's continuous free oscillations by atmosphere-ocean-seafloor coupling, *Nature*, *431*, 552–556.

Rhie, J., and B. Romanowicz (2006), A study of the relation between ocean storms and the Earth's hum, *Geochem. Geophys. Geosyst.*, *7*, Q10004, doi:10.1029/2006GC001274.

Shchepetkin, A. F., and J. C. McWilliams (2005), The Regional Oceanic Modeling System: A split-explicit, free-surface, topography-following-coordinate oceanic model, *Ocean Modell.*, *9*, 347–404.

Sheremet, A., R. T. Guza, S. Elgar, and T. H. C. Herbers (2002), Observations of nearshore infragravity waves: Seaward and shoreward propagating components, *J. Geophys. Res.*, *107*(C8), 3095, doi:10.1029/2001JC000970.

Suda, N., K. Nawa, and Y. Fukao (1998), Earth's background free oscillations, *Science*, *279*, doi:10.1126/science.279.5359.2089.

Symonds, G., D. A. Huntley, and A. J. Bowen (1982), Two-dimensional surf beat: Long wave generation by time varying breakpoint, *J. Geophys. Res.*, *87*(C1), 492–498.

Tanimoto, T. (2005), The oceanic excitation hypothesis for the continuous oscillation of the Earth, *Geophys. J. Int.*, *160*, 276–288.

Tanimoto, T., and J. Um (1999), Cause of continuous oscillations of the Earth, *J. Geophys. Res.*, *104*(B12), 28,723–28,739.

Tanimoto, T., J. Um, K. Nishida, and N. Kobayashi (1998), Earth's continuous oscillations observed on seismically quiet days, *Geophys. Res. Lett.*, *25*(10), 1553–1556.

Tucker, M. J. (1950), Surf beat: Sea waves of 1 to 5 min. period, *Proc. R. Soc. London, Ser. A*, *202*, 565–573.

Ursell, F. (1952), Edge waves on a sloping beach, *Proc. R. Soc. London, Ser. A*, *214*, 79–97.

Webb, S. C. (1998), Broadband seismology and noise under the ocean, *Rev. Geophys.*, *36*, 105–142.

Webb, S. C. (2007), The Earth's "hum" is driven by ocean waves over the continental shelves, *Nature*, *445*, 754–756.

Webb, S. C., X. Zhang, and W. Crawford (1991), Infragravity waves in the deep ocean, *J. Geophys. Res.*, *96*(C2), 2723–2736.

J. C. McWilliams and Y. Uchiyama, Institute of Geophysics and Planetary Physics, University of California, Los Angeles, 3845 Slichter Hall, Los Angeles, CA 90095-1567, USA. (uchiyama@atmos.ucla.edu)